Master thesis and internship[BR]- Master thesis : Investigation of Analytical Models for Evaluating the Impact of Distortion on Compressor Performance and Stability[BR]- Integration internship

Auteur : Escudero Saiz, Alvaro
Promoteur(s) : Hillewaert, Koen
Faculté : Faculté des Sciences appliquées
Diplôme : Master en ingénieur civil en aérospatiale, à finalité spécialisée en "aerospace engineering"
Année académique : 2019-2020
URI/URL : http://hdl.handle.net/2268.2/8641

UNIVERSITY OF LIÈGE

FACULTY OF APPLIED SCIENCES

INVESTIGATION OF ANALYTICAL MODELS FOR EVALUATING THE IMPACT OF DISTORTION ON COMPRESSOR PERFORMANCE AND STABILITY

Graduation Studies conducted for obtaining the
Master's degree in Aerospace Engineering

by:

ÁLVARO ESCUDERO SAIZ

Promotor: Mr. Koen Hillewaert (University of Liège)
Co-Promotor: Mr. Patrick Hendrick (Free University of Brussels)

Academic year 2019/20

Acknowledgements

First and foremost I offer my sincerest gratitude to my academic supervisors, Mr. Koen Hillewaert and Mr. Patrick Hendrick, who gave me the opportunity to perform this Master Thesis in a collaboration between the University of Liège and the Free University of Brussels.

I really admire the devotion and the dedication that you give to your students, sharing with us your knowledge and experience. In the same way, I would like to extend this thanks to all those professors and educators who gave their best to help me grow.

I would like to pay my greatest thanks to my friends that I have made during during all these years of education in Madrid, Liège and Brussels. Thank you for your support and help, specially in the toughest moments that we have shared together.

Finally, a very special thanks to the most important, José, Vega and specially my parents. You have always trusted me and supported me, being my best reference; so I will always be really grateful for it.

Thank you.

Contents

List of Figures

List of Tables

1 Introduction

1.1 Summary

The aim of this study is to estimate the effect of different non-uniformities in performance and stability of compressors. Three types of distortion have been included: pressure, swirl and temperature. While pressure and swirl distortion may occur in both civil and military aircraft, temperature distortion uses to appear only in military applications.

Firstly, distortion index generated by non-uniformities in different pressure profiles at the Aerodynamic Interface Plane (AIP) have been calculated. Several ways to model the distortion pattern have been used. Radial and circumferential distortion indexes have been calculated using the guideline of the Society of Automotive Engineers (SAE), which have been proposed in order to unify criteria between engineer manufacturers. However, each manufacturer continues to use its own indexes. As an example, two more indexes developed by Pratt & Whitney are used to mix both radial and circumferential indexes and understand the effect of combined distortion.

Once the distortion is defined, it is related with the stability of the engine against surge. To analyze the behavior of the engine operating with distortions, the Parallel Compressor Model (PCM) has been implemented in MATLAB. This model has been applied to a low pressure compressor map. Surge points of clean and distorted conditions have been calculated, what has allowed to obtain surge margin for each one. Since variations in distortion give rise to changes in the surge margin, both can be related. Evolution of surge margin with both corrected speed and distortion index are presented.

A similar procedure has been performed in the case of swirl distortion. Some parameters have been defined to characterize the distortion that is present at the AIP and changes in speed lines due to swirl distortion have been calculated with a Mean Line Code (MLC). This code has been implemented in MATLAB and it has been used with an example rotor, for which changes in performance and stability have been estimated for different swirl angles.

Finally, effects of temperature have been computed with a modified version of the Parallel Compressor Model (PCM) for temperature distortion. This model has been applied to a low compressor map and results calculated have been compared with those obtained experimentally. Furthermore, the evolution of surge margin with distortion index has been computed.

1.2 Why to study distortion?

Inlet distortion is a critical issue for current and future aircraft architecture. Understanding aerodynamics under distortion is essential to design distortion-tolerant fan systems. Stable compressor operation even under adverse conditions is necessary to the functioning of any gas turbine engine. However, the compressor could be vulnerable to some flow non-uniformities such as rotating stall or surge due to the different flows which can enter through the air-intake.

Rotating stall appears when a large stall zone covers some blades of the compressor. The number of stall zones and the propagating rates vary considerably, depending on the root of the stall and its propagation. The propagation mechanism is shown in figure 1 and can be described by considering the blade row to be a cascade of blades. A flow perturbation causes

blade 2 to reach a stall before the other blades. This stalled blade does not produce enough pressure rise to maintain the flow around it, and an effective flow blockage appears.

This retarded flow diverts the flow around it so that the angle of attack increases on blade 3 and decreases on blade 1. In this way, the stall propagates downward relative to the blade row at a rate about half the rotational speed; which result in stall apparition in the blades below the retarded-flow zone and stall remove from the blades above it. The relative speed of propagation has been observed from compressor tests to be less than the rotor speed. Observed from an absolute frame of reference, the stall zones appear to be moving in the direction of rotor rotation. The radial extent of the stall zone may vary from just the tip to the whole blade length.

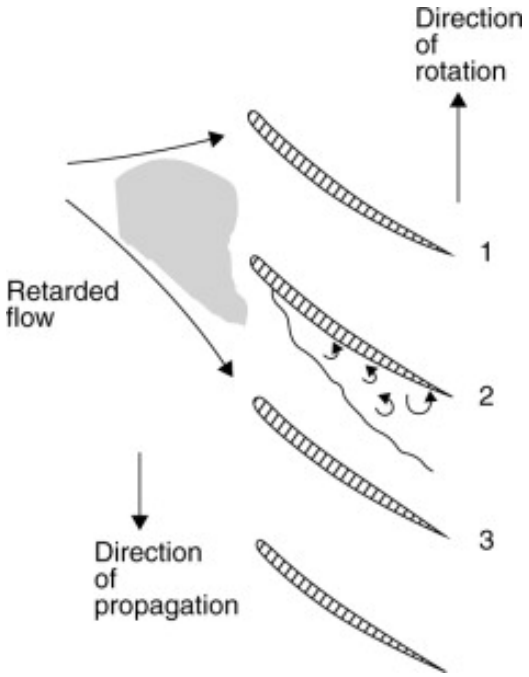

Figure 1: Stall apparition and propagation. Reproduced from Boyce [1]

Compressor surge is an instability that typically follows the appearance of rotating stall. On a constant speed line, corrected airflow decreases when the pressure ratio increases, so the internal flow is in a higher adverse pressure gradient, which makes it harder to reach the high pressure zone, destabilizing it and leading to its separation.

Surge results in a total loss of thrust and it is a much more dangerous event than a partial loss of thrust due to a reduction of compressor efficiency. Violent flows that occur during surge hit the blades, giving rise to structural problems such as blade fatigue or mechanical failure. Specifically, very large transverse loads on the blades and casing appear during the initial transient process that initializes surge.

This instability also leads to flameout, due to the not-burned fuel which arrives to the exit of the engine, where oxygen is enough. This not-burned fuel appear due to the lack of oxygen in the combustion chamber. Strong vibrations and noises are other kind of problems that may appear during surge.

1.3 Objectives

The main aim of this particular project was to understand the flow physics of how various types of distortion affect the turbomachinery aerodynamics, and consequently result in the undesirable instabilities, such as the onset of rotating stall and/or surge.

Overall the objective was to develop a kit of fast analytical tools in order to correlate, through the appropriate flow descriptors, the loss in stability pressure ratio due to different types of distortion. Within this context, the following tasks were accomplished:

1. Characterize pressure distortion using different distortion indexes, analyze pressure maps with image processing and compute its distortion index.
2. Relate distortion indexes with compressor behaviour and simulate the effects of pressure distortion on compressor performance and stability.
3. Define swirl distortion and evaluate its influence on compressor performance and stability. Relate distortion descriptors with compressor behaviour.
4. Characterize temperature distortion and simulate its effects on compressor performance and stability.
5. Create a kit of tools to evaluate quickly the effect of different types of distortion. Implement analytical models in MATLAB to simulate compressor behaviour in these conditions.

Table 1 summarizes these tasks in terms of objectives and the proposed analytical solutions to reach them.

Objective	**Solution**
Characterize and compare distortion	Distortion Indexes
Effect of pressure distortion	Parallel Compressor Model
Effect of swirl distortion	Mean Line Code
Effect of temperature distortion	Parallel Compressor Model for temperature

Table 1: Objectives of the project and proposed solutions to achieve them.

1.4 State of the art

Engineers worked hard in gas turbine engines during 1940s and 1950s, but it is during 1960s when distortion phenomena was taken into account due to the effects that it could cause in the performance and stability of the engine. First studies were focused on pressure distortion, while studies about temperature distortion and swirl distortion started later.

Pearson and McKenzie proposed the parallel compressor model [14] in an first attempt to analyze compression system performance and stability variations with inlet distortion. Quickly, this model was used by other engineers and is still used for fast calculations (with some modifications). It is a good tool to have an idea of the influence of pressure distortion on compressor behaviour, even results are not too accurate. Some years later, Reid introduced a big change in the model [15] for low distortion angles, where the model developed by Pearson and McKenzie did not follow the behaviour of the compressor.

During these years, engineers characterized inlet distortion with simple mathematical models and data from tests. Each manufacturer developed its own indexes, which made difficult communication and comparison between engines. The Society of Automotive Engines created the S-16 committee, whose final work was an aerospace recommended practice (ARP-1420) [3].

The goal was to homogenize this nomenclature and solve the problem but, finally, the majority of manufacturers are still using their own indexes. To evaluate the different distortion indexes, Campbell did a research where some of them were compared [16]. Indexes studied were:

- ARP-1420 method from Society of Automotive Engines.
- Pratt & Whitney KD_2 and KA_2 indexes.
- Common $\Delta P/P_{AVG}$ indexes.
- General Electric Method D system.
- Naval Air Propulsion Center K_θ.
- Rolls Royce θ critical indexes.
- AVCO Lycoming DI index.
- Garrett AiResearch CDI index.

This research did not find any index that fits better with experimental results, but ARP-1420 was able to provide consistently good correlations. Also, indexes proposed by this aerospace recommended practice have been typically used in research papers and technical documents open to scientific community.

Total pressure distortion focused the effort of engineers and scientist for many years, but total temperature distortion later became an interesting area due to the military applications where it may appear. Some examples are gun and rocket gas ingestion, vertical take-off or aircraft carrier operation. In commercial applications, thrust reverser operation during landing and ingestion of hot gases from other aircraft in runway situations are other examples.

In 1991, S-16 Committee presented an aerospace resource document (ARD) about temperature distortion, which analyzed the effect of temperature distortion in a similar way than the one presented before for total pressure distortion.

Concerning to swirl distortion, it was thought to be predominately induced by the pressure distortion and its contribution to flow distortion was assumed small in comparison with total pressure distortion. However, the Tornado aircraft case showed that moderate pure bulk swirl at the inlet, generated by the S-shaped duct, could lead to surge.

In the same way as in the previous cases of total pressure and total temperature distortion, S-16 Committee created a guideline to characterize swirl distortion [11]. Even so, these techniques are still in early stages of development because of the little knowledge about swirl distortion phenomena.

First techniques based on experimental tests and simple analytical models evolved due to the advance of computational fluid dynamics (CFD) methods, specially after 1990s. The main advantage of CFD is the accuracy of results which can be obtained, although it requires a high computation power. Results obtained with CFD are compared with those obtained experimentally with tests.

In recent years almost all companies which are working in aeronautical fields have incorporated specialized software to simulate accurately their models. Researchers and scientists also use CFD as it is shown in some papers and thesis (Haug et al. [17], Mehdi [10], Kaili et al. or [18], Naseri et al. [19]).

Nowadays, there are some international projects focused on reducing emissions such as Clean Sky Project or Advanced Air Transport Technology (AATT) Project. The aim of these projects is to enable aircraft with improved energy efficiency, environmental compatibility and economic impact. AATT project defined some objectives in terms of noise, emissions and consumption which are shown in table 2.

TECHNOLOGY BENEFITS	Technology generations (Technology Readiness Level = 5-6)		
	Near Term (2015-2025)	Mid Term (2025-2035)	Far Term (beyond 2035)
Noise (cum below Stage 4)	22 - 32 dB	32 - 42 dB	42 - 52 dB
LTO NO_X Emissions (below CAEP 6)	70 - 75 %	80 %	>80 %
Cruise NO_X Emissions (rel. to 2005 best in class)	65 - 70 %	80 %	>80 %
Aircraft Fuel/Energy Consumption (rel. to 2005 best in class)	40 - 50 %	50 - 60 %	60 - 80 %

Table 2: Objectives of the AATT project in terms of noise, emissions and consumption.

In September 2019, 24th Conference of the International Society for Air Breathing engines was celebrated in Canberra, Australia. One of the key topics was the use of boundary layer ingestion (BLI) to reduce fuel burn, aircraft wetted area and wake mixing losses. Works of different companies and researchers related with BLI were presented, such as Celestina et al. [2], Lee et al. [20] or Kagaya et al. [21].

One configuration that uses BLI is the Hybrid Wing Body (HWB) vehicle shown in figure 2. Results obtained in preliminary studies estimate a reduction in fuel consumption between 3 % and 5 %, with potential to reach reductions around 10 % in far-term configurations with larger amounts of BLI [22].

There are two types of BLI configurations depending on the integration between propulsor and fuselage. Type I is characterized by a flat boundary layer which is ingested and it results in a low total pressure region with presence of swirl distortion over the bottom part of the inlet while the upper part has constant total pressure and no swirl distortion. Type II is characterized by an axisymmetric boundary layer developed along the fuselage, the ingestion wing upwash and the effect of the vertical tail. This distortion presents an inlet with low total pressure and large variation at the hub. To date, NASA AATT has only completed experimental tests of the Type I distortion (Type II is in progress).

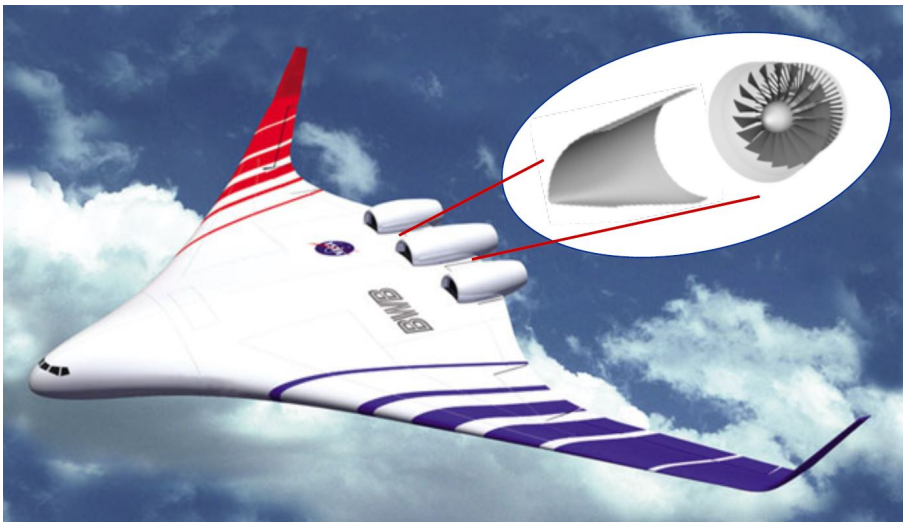

Figure 2: Embedded boundary layer ingesting propulsion system for hybrid wing body aircraft. Reproduced from Celestina et al. [2]

Therefore, use BLI to reduce fuel consumption and emissions means to deal with distortion effects, so it is necessary to understand these effects in compressor performance and stability. Clean Sky Project is a public-private partnership between the European Commission and some private companies that coordinates and funds research activities focused on reduce fuel consumption and emissions. These activities are carried out in universities and research centers and some of them related with the study of distortion and its effect on compressor behaviour.

In this context, and following the actual trends, this Master Thesis carried out at the University of Liège and the Free University of Brussels presents an overview of distortion. Total pressure, swirl and total temperature have been studied and a kit of tools to analyze the effect of these types of distortion has been developed.

During the realization of this project, a collaboration with the Von Karman Institute for Fluid Dynamics has started. One of the projects of this research center aims to understand the evolution of distortion across the compressor. The objective of this collaboration is to use the tools developed on this thesis to predict compressor behavior trends in some distortion conditions and to compare the results presented with future results obtained through CFD or experimental tests.

2 Pressure Distortion - Distortion Indexes

Pressure distortion occur in a wide variety of occasions such as complex geometry ducts, high angle of attack, ground vortices, wakes from stalled wings, etc. In a first approximation, distortion patterns can be separated in radial and circumferential, which are calculated using the guidelines of Society of Automotive Engineers (SAE).

2.1 Data management

CFD images of different pressure profiles at the AIP have been chosen from reference [4]. From these images, some points have been chosen to be studied. Each image has been divided in 10 sectors and 10 rings, so 100 points have been used in each image.

Each point should represent the same amount of mass flow rate $\dot{m}$ in order to represent the same influence to calculate the distortion generated by this point. For this reason, each point has to represent the same area of the AIP. This is why each of the 10 sectors has the same amplitude (36°) and the rings' position has been calculated to keep the area associated to each point point. The position of the rings is given in percentage of the total radius and it is represented in table 3.

Ring	1	2	3	4	5	6	7	8	9	10
Position (% R)	15.9	38.4	50.0	59.3	67.3	74.5	80.9	87.0	92.6	97.9

Table 3: Radius of each ring in % of total radius.

2.2 Circumferential distortion index

Circumferential distortion index (CDI) is described on a ring-by-ring basis and it is defined in terms of intensity, extent and multiple-per-revolution elements. The intensity or level of distortion is an indicator of the magnitude of the pressure distortion. The extent (or spoiled angle) is an indicator of how large is the region whose pressure is less than the average pressure, which will be the distorted region. The multiple-per-revolution is an indicator of how many regions of low pressure exist in the studied ring.

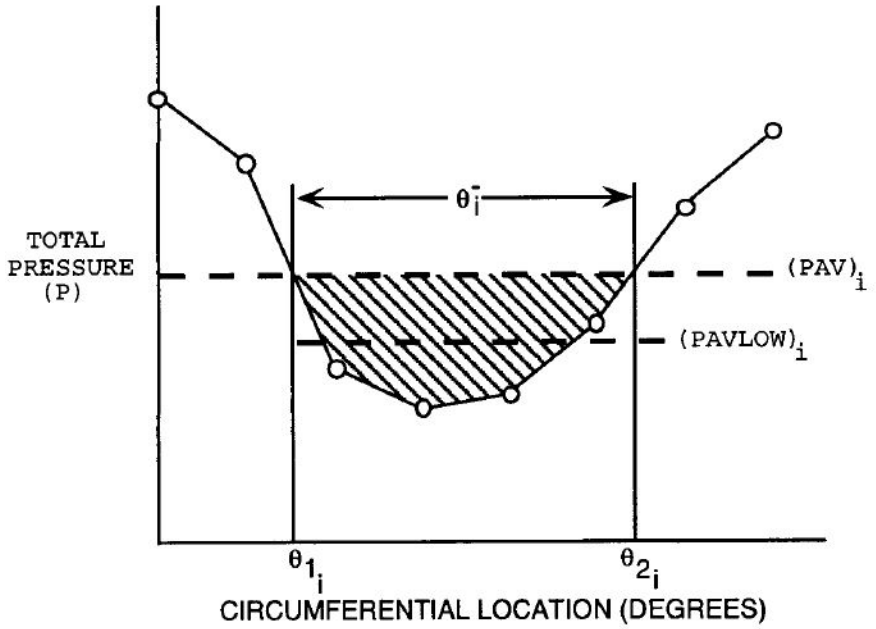

Figure 3: Ring Circumferential Distortion for a One-Per-Revolution Pattern. Reproduced from SAE [3].

In a one-per-revolution pattern, both intensity and extent of circumferential distortion are calculated by linear interpolation of the different points of the ring. Figure 3 shows a typical pressure distribution of one ring, where the average pressure, the area of the distorted region, the average pressure of this low pressure region and its extent are represented. These values are calculated with the next equations, given by reference [3]:

$$\theta_i^- = \theta_{2i} - \theta_{1i} \tag{1a}$$

$$CDI = \left(\frac{\Delta PC}{P}\right)_i = \left(\frac{P_{AV} - P_{AVLOW}}{P_{AV}}\right)_i \tag{1b}$$

$$P_{AVi} = \frac{1}{360}\int_0^{360} P(\theta)_i \, d\theta \tag{1c}$$

$$P_{AVLOWi} = \frac{1}{\theta_i^-}\int_{\theta_{1i}}^{\theta_{2i}} P(\theta)_i \, d\theta \tag{1d}$$

$$\tag{1e}$$

In a multiple-per-revolution pattern, there is more than one region with lower pressure than the average pressure. Figure 4 shows a typical pressure distribution of one ring. In this case, it is necessary to determine the critical low pressure region, which will be the one whose value of $(\Delta \mathrm{PC/P})_{i,k} \cdot \theta_{i,k}^-$ (for k low pressure regions) is maximum. Once this region is defined for each ring, its circumferential distortion and its extent will be calculated using equations 17.

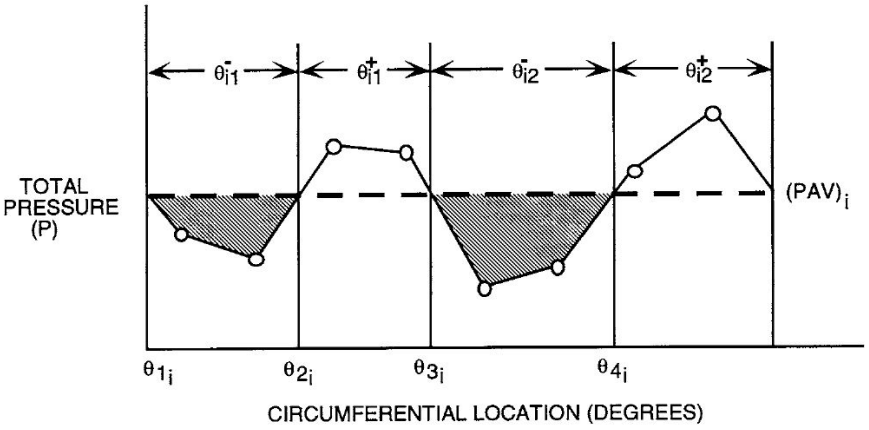

Figure 4: Ring Circumferential Distortion for a Multiple-Per-Revolution Pattern. Reproduced from SAE [3].

2.3 Radial distortion index

The radial distortion index (RDI) is defined as the difference between the average pressure of the ring and the average pressure of the AIP. It is possible to have both positive and negative values, where positive values refer to the rings whose pressure is lower than the average. For the general ring, i, the radial intensity is given also by reference [3]:

$$\left(\frac{\Delta PR}{P}\right)_i = \frac{P_{AIP} - P_{AVi}}{P_{AIP}} \tag{2}$$

2.4 KD_2 distortion index

This index was developed by Pratt & Whitney and represents a first point that considers both circumferential and radial distortion. It is defined as follows [23]:

$$KD_2 = \frac{\sum_{i=1}^{k} \left[\frac{\Delta PC}{P}\theta^-\right]_i \frac{1}{D_i}}{\sum_{n=1}^{i} \frac{1}{D_i}}$$

Where:

- θ^- is the extent angle of the low pressure region.
- D_i is the diameter of the selected ring.

However, even it takes in count the radial position of each ring, this index refers mainly to circumferential distortion; so a new index has been defined to better take into account the influence of the radial distortion.

2.5 KA_2 distortion index

This index was also developed by Pratt & Whitney and it considers both circumferential (K_θ) and radial (K_{rad}) distortion through the parameter b, which is the radial distortion weighting factor [24]:

$$KA_2 = K_\theta + bK_{rad} \tag{4}$$

This factor was developed for the F-100 engine, which is an afterburning turbofan engine that powers the F-15 Eagle and F-16 Fighting Falcon. Radial distortion weighting factor depends on the mass flow rate, and its values are shown in figure 5. These values have been taken from reference [25]. To approximate the experimental points, a Fourier's series has been used.

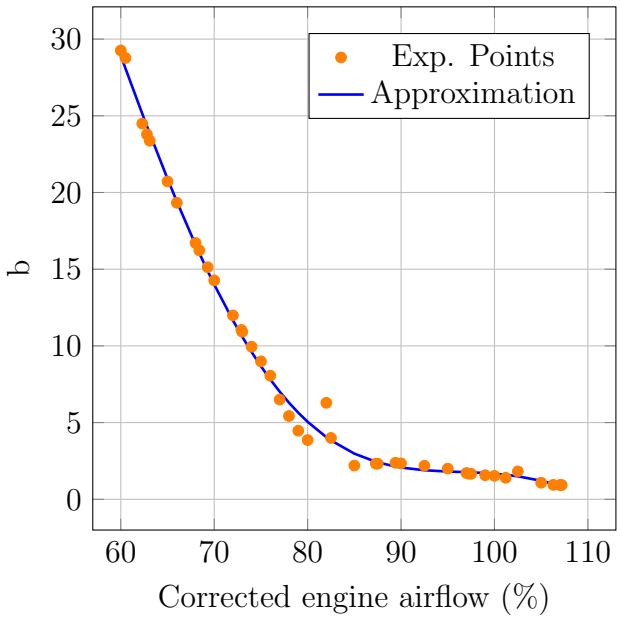

Figure 5: Evolution of b Factor with corrected engine airflow.

It is important to remark that these values have been taken for F100 engine, so other engines will have different values of b factor. Military engine values are similar than those showed before, while civil engines values are more different.

Circumferential distortion component of this index is defined as follows:

$$K_\theta = \frac{\sum_{i=1}^{k} \left[\left(\frac{a_N}{N^2} \right)_{max} \right]_i \frac{1}{D_i}}{\left(\frac{q}{P_{T2}} \right)_{ref} \sum_{n=1}^{i} \frac{1}{D_i}} \tag{5}$$

Where,

- a_N are the coefficients of the Fourier's Series which represents the evolution of the pressure in each ring. Figure 6 shows an example of how this approximation fits the real pressure distribution in ring 5 of example 1.
- q/P_{T2} is the reference value of AIP dynamic pressure head, function of AIP Mach number.

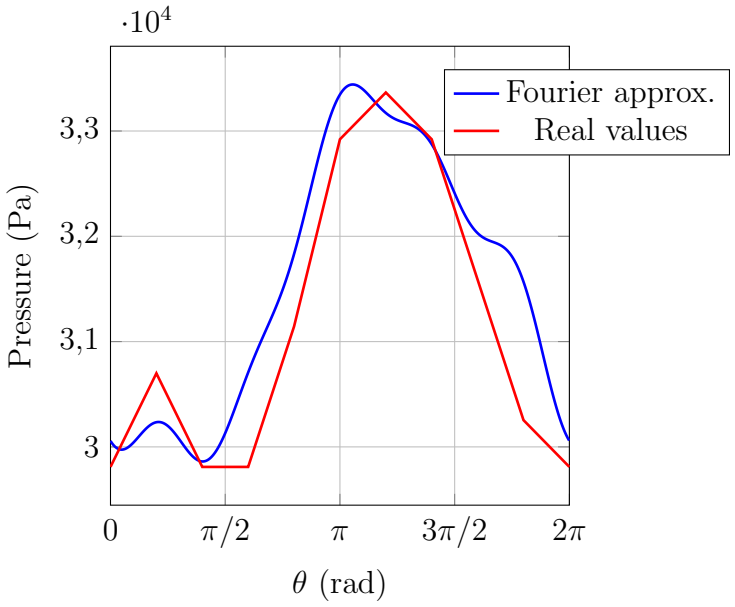

Figure 6: Fourier's Series approximation for one ring pressure evolution.

Radial distortion component can be expressed by:

$$K_{rad} = \frac{\sum_{i=1}^{k} \left(\frac{\Delta P_{T2}}{P_{T2}}\right)_i \frac{1}{D_i}}{\left(\frac{q}{P_{T2}}\right)_{ref} \sum_{n=1}^{i} \frac{1}{D_i}} \tag{6}$$

Where,

$$\frac{\Delta P_{T2}}{P_{T2}} = \left| \frac{\left(\frac{P^*_{T2}}{P_{T0}}\right)}{\frac{P_{T2}}{P_{T0}}} - \frac{P^*_{T2,base}}{\bar{P_{T2}}} \right| \frac{\bar{P_{T2}}}{P^*_{T2,base}} \tag{7}$$

and

- P^*_{T2}/P_{T0} is the ring average pressure recovery.
- P_{T2}/P_{T0} is the face average pressure recovery.
- $P^*_{T2,base}/\bar{P_{T2}}$ is the reference radial profile, function of the corrected engine airflow and the radius of the ring.

2.6 Results

Four images from reference [4] have been studied. These images are four AIP where different pressure maps have been represented, trying to cover a wide variety of possibilities in terms of distortion patterns.

To compute the distortion indexes, an image analysis code has been developed and implemented in MATLAB. This code obtains the total pressure value of 100 points circumferentially and radially distributed according to chapter 2.1, selecting each point so that everyone has the same associated airflow.

Both first and second pressure maps represent a circumferential distortion pattern, where low pressure critical region is higher in the second one. In the third example, the circumferential distortion is small while the radial distortion is more important than in both examples before. Even, variations of pressure are not large in all the pressure map. The fourth pressure map shows a radial distortion pattern.

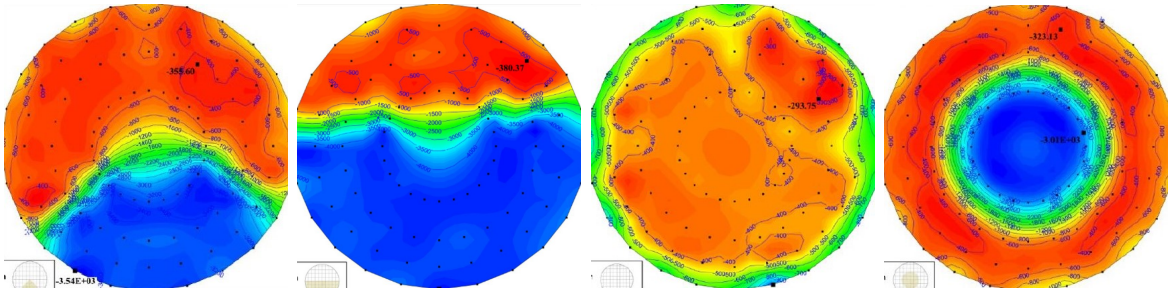

(a) Ex. 1 (b) Ex. 2 (c) Ex. 3 (d) Ex. 4

Figure 7: Studied distortion patterns. Reproduced from Pecinka et al. [4].

Selected flight conditions are:

- Altitude $\rightarrow$ h = 11.000 m $\rightarrow$ P_0 = 22.600 Pa
- Mach $\rightarrow$ M = 0.8 $\rightarrow$ P_{T0} = 34.500 Pa
- Ram Recovery $\rightarrow$ RR = 0.98 $\rightarrow$ P_{T2} = 33.800 Pa
- Corrected engine airflow $\rightarrow$ $\dot{m}_{corr}$ = 100 % $\rightarrow$ b = 1.5

2.6.1 Circumferential and radial distortion

These distortion indexes are calculated for each ring, so its evolution its shown in next figures.

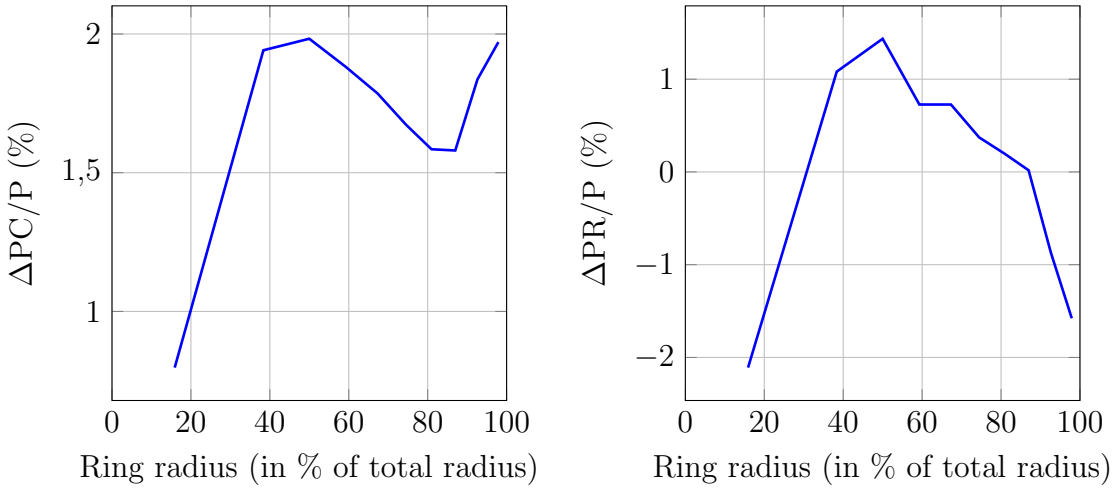

Figure 8: Circumferential and radial distortion of example 1.

Example 1 presents a circumferential distortion pattern with a low pressure region of 120^{o} approximately. According to this, circumferential distortion index is important, while radial distortion has less importance. Figure 8 demonstrates it by showing how the circumferential index reaches high values; while radial distortion is less important due to its small value.

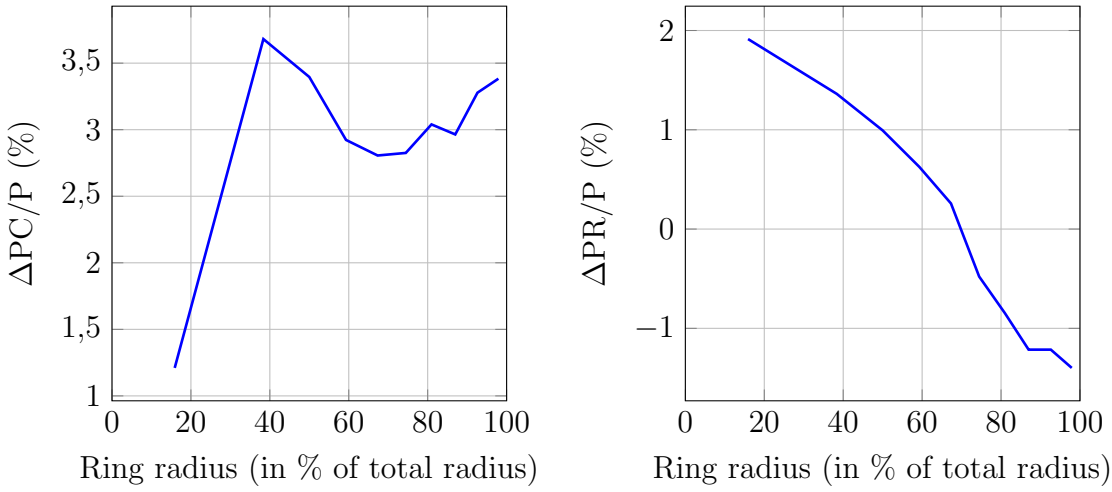

Figure 9: Circumferential and radial distortion of example 2.

Example 2 is similar to the first one, with a higher extent of low pressure region. In the same way as in the previous case, figure 9 shows that circumferential distortion index is high (even larger than example 1) and radial distortion index is low. In both first and second examples, circumferential distortion is more important than radial distortion.

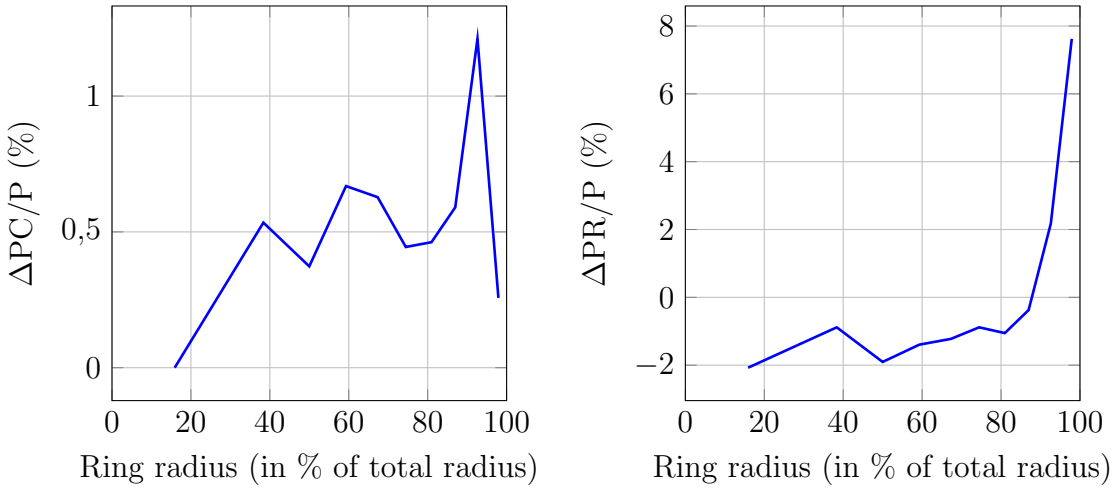

Figure 10: Circumferential and radial distortion of example 3.

Example 3 shows a different distortion pattern. In this case, there is a large percentage of area in which the pressure variation is low. Near the ends of the duct there is a decrease in pressure and there is also a small region of high pressure in the upper right corner. It is expected that radial distortion is more important than circumferential in this case.

Figure 10 shows that circumferential distortion values are low, below 0.2 % in most rings; while radial distortion presents a peak near the duct. This matches what was expected, because the peak in ΔPR/P is related to the decrease in pressure near the end of the duct.

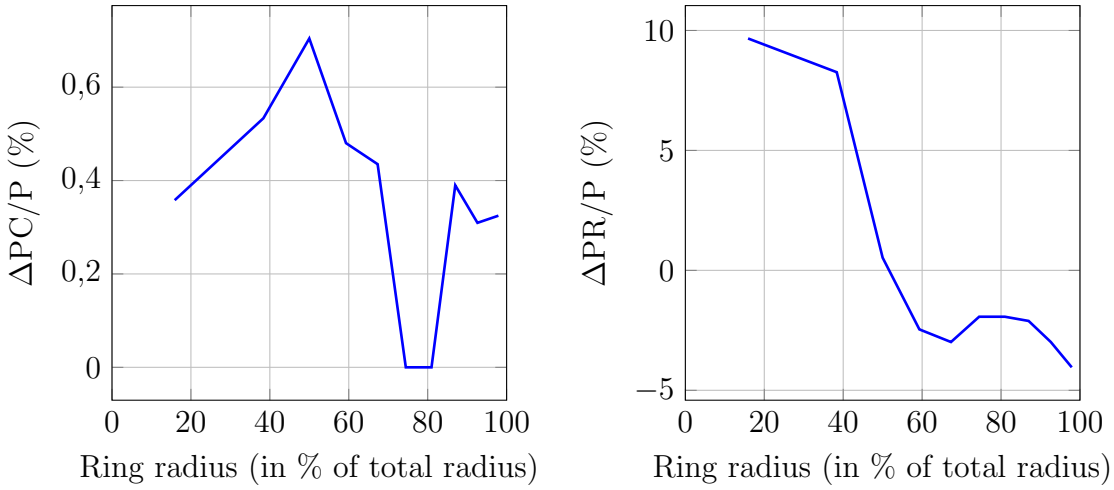

Figure 11: Circumferential and radial distortion of example 4.

Example 4 presents a radial evolution of the pressure, which has low values in the center of the duct, and high values near the end of the duct. Figure 11 shows that circumferential distortion is low, with some rings of constant pressure where circumferential distortion index is zero. Radial distortion index represents the evolution described above, where high values of ΔPR/P are related with the inner duct area of low pressure, low values of ΔPR/P are related with the outer duct area of high pressure and the intermediate region where ΔPR/P decreases quickly refers to the transition region between the previous two.

It is possible to summarize circumferential distortion index either with the average value CDI_{mean} or with the maximum value CDI_{max}. In this way, a single value characterizes the distortion present throughout the AIP, which will subsequently be related to the surge margin as in the later example in which the evolution of the surge margin with CDI_{mean} is shown.

	CDI_{mean} (%)	**CDI_{max} (%)**
Ex. 1	1.70	1.98
Ex. 2	2.95	3.68
Ex. 3	0.52	1.21
Ex. 4	0.35	0.70

Table 4: Values of CDI_{mean} and CDI_{max} for the examples of figure 7.

Values of CDI_{mean} and CDI_{max} are presented in table 4. According to the above, examples 1 and 2 present higher values of circular distortion index, while examples 3 and 4 have lower values. Between examples 1 and 2, the second one has a larger circular distortion index so it will be the one that presents a smaller surge margin.

2.6.2 KD_2 and KA_2 distortion

KD_2 is an index that well represents the circumferential distortion, but it attenuates the effect of radial distortion. Hence, this index does not provide accurate information for calculating the distortion index of a pressure map.

KA_2 is a more developed index that calculates circumferential and radial distortion separately and then, it includes both through the b parameter, which depends on the corrected engine airflow, as it was shown in figure 5. The values obtained for the indexes presented above for each pressure map are:

	KD_2 (%)	**K_θ (%)**	**K_{rad} (%)**	**KA_2 (%)**
Ex. 1	5.1	1.6	21.7	33.9
Ex. 2	5.3	1.7	24.6	38.4
Ex. 3	0.1	0	18.6	28.2
Ex. 4	0.5	0.1	31.5	47.6

Table 5: Values of the presented distortion indexes for the examples of figure 7.

KD_2 is high in both first and second examples, where circumferential distortion is important; while is close to zero in examples which present low circumferential distortion patterns. This explanation is also valid for the circumferential component K_θ of the KA_2 index.

To understand the behaviour of K_{rad}, it is a good idea to study its definition, given before in equation 6. For a given condition of corrected engine airflow, altitude and Mach, it is only the first term of the division, $\Delta P_{T2}/P_{T2}$, that changes between pressure maps. This term depends on the relation between the ring pressure recovery average and the face pressure recovery average, and it is also influenced by the number of rings in which the relation mentioned is important.

On the one hand, in pressure maps in which circumferential patterns are dominant, all rings contribute to the same extent to increase the $\Delta P_{T2}/P_{T2}$ ratio, so the final value of this relation is usually large, as it is shown in table 5 for first and second example.

On the other hand, pressure maps in which radial patterns are dominant, only some rings contribute to increase $\Delta P_{T2}/P_{T2}$, but the contribution of each is usually large compared with the contribution in the previous case. However, the final value of the ratio studied depends on the number of rings that contribute, that is, of the area of the low pressure region.

Although first and second examples present circumferential patterns, both two have a high value of radial distortion, which lead to a large value of KA_2. In the third example, where the value of the pressure is, for the most part, close to the average; it presents the lower value of KA_2, that is mainly due to the decrease in pressure near the end of the duct. The fourth example presents a radial distortion pattern, In which the central region has low pressure while the outer region has high pressure. In this case, KA_2 reaches its higher value.

2.6.3 Sensitivity Analysis of KA_2

KA_2 index depends on the altitude, the Mach number. Figure 12 shows the evolution of KA_2 with these magnitudes for the example 1 of figure 7.

When the altitude increases the ambient pressure drops, and also the total pressure, so the same amount of distortion over a lower average pressure translates into an increase in the distortion index. Since the pressure decreases exponentially with altitude, the distortion index KA_2 increases also exponentially. It can be concluded that, in case of high altitudes, if a KA_2 value that endangers the operation of the engine is reached, a flight roof with enough safety margin must be fixed to avoid problems in flight.

Increasing the Mach results in an exponential increase in total pressure. Following the example of the previous case, when total pressure increases distortion decreases so, for higher Mach numbers, KA_2 will decrease. A minimum Mach associated with a safe value of the distortion index should be warranted to ensure proper engine operation.

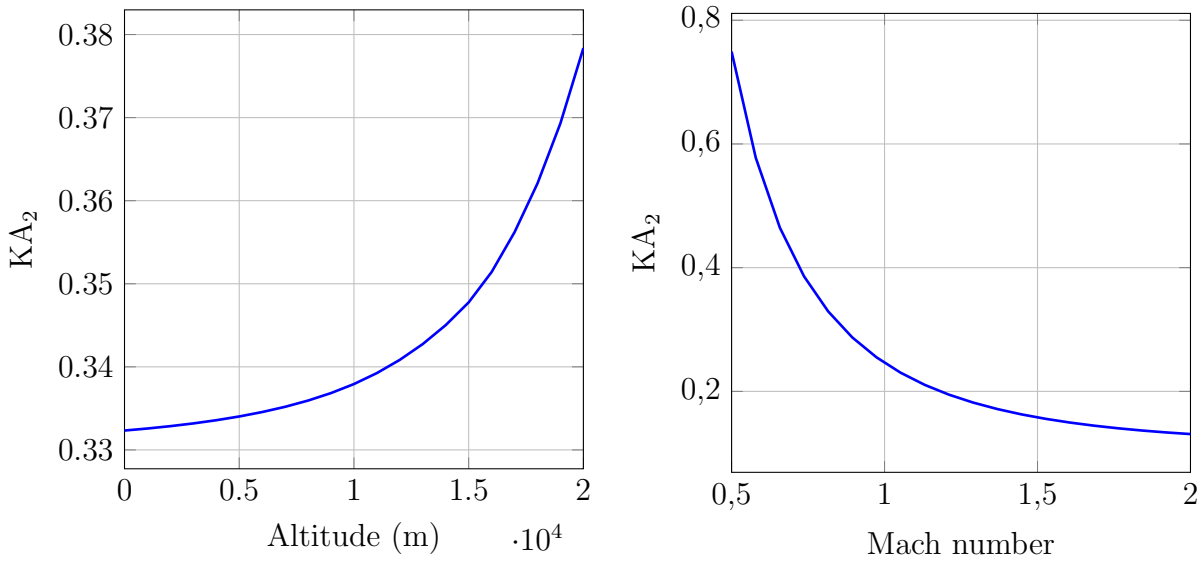

Figure 12: Variation of KA_2 with altitude and Mach.

2.7 Summary of Distortion Indexes

Distortion indexes have different characteristics. Some of them represent better circumferential distortion, while others are better representing radial distortion while it is possible to find more complex indexes that are able to represent both circumferential and radial distortion together.

During this chapter, some distortion indexes have been presented; each one with its advantages and disadvantages; and they have been used to evaluate the distortion in different distortion maps from figure 7. According to the results obtained, table 6 shows the adaptation of each one to different distortion patterns.

	CDI	**RDI**	**KD_2**	**KA_2**
Circular pattern	✔	✖	✔	✔
Radial pattern	✖	✔	✖	✔
Circular and radial pattern	✖	✖	✖	✔

Table 6: Comparison between distortion indexes and how fit with distortion patterns.

On the one hand, Circular Distortion Index (CDI) fits better circular distortion patterns, while results obtained with radial or mixed distortion patterns do not represent the amount of distortion accurately. On the other hand, Radial Distortion Index (RDI) fits better radial distortion patterns than the others.

KD_2 is a first attempt to mix both radial and circumferential distortion in one index, but results are acceptable only for circumferential distortion pattern. The reason why this results are not accurate in all situations, even when this index considers radial position of each ring, is because it is focused mainly in circumferential distortion.

Finally, KA_2 is able to collect both radial and circumferential effects present in a pressure map. However, this is a complex index that needs more data (some of them obtained experimentally) to be computed. Besides, it is only used by Pratt & Whitney engineers so it is difficult to find information and public results where KA_2 is related with the effect of distortion on compressor performance and stability.

Since most of the open information that relates distortion indexes and compressor behavior is in terms of Circular Distortion Index and this is the index proposed by the S-16 Committee to homogenize the study of distortion, CDI has been used in this thesis to characterize circular distortion patterns.

3 Effect of pressure distortion on compressor stability

During operation, the engine uses to work with an homogeneous pressure and temperature map at the Aerodynamic Interface Plane. However, sometimes different flows can change the pressure or temperature map leading to distortion. This phenomenon is very important in terms of engine stability because surge may occur if distortion is not controlled.

Surge is an instability which starts with stall and results in the complete disruption of the airflow through the compressor. If surge happens, there is a loss of compression and flame shutdown that disables the engine, which should be turned off and re-started. Also, this instability can lead to structural damages.

One method to analyze the effect of distortion on the stability engine is using the parallel compressor model, where the distorted pressure map is divided in two clean regions of high and low values which are studied separately. Surge in distorted compressor will occur when any of the regions reaches it.

3.1 Parallel compressor model

This model was developed during the 60s, but it is still in use nowadays. It has been used by many authors as Milner [26], Kurzke [13], Cousins [12] or Pokhrel [6]; so it has been considered as a good option to model the behaviour of the compressor under distortion conditions.

The model considers a circular distorted pattern with two regions, which lead to two virtual compressors that work in parallel. Each compressor has uniform pressure, one with the value of the low pressure region and the other with the value of the high pressure region. Both compressors discharge to the same static pressure, which makes the relation of how work together.

Observations made by Rolls-Royce regarding the influence of radial distortion and circumferential distortion on surge have been taken as a reference to assess the suitability of this model for the problem posed. The main conclusion of these studies carried out to evaluate the tolerance of different engines against distortion is that circumferential distortion is much more detrimental to the stability of the compressor than radial distortion.

Airflow through each compressors depends on the extent of each region so, if the low pressure region is $60^o/360^o = 1/6$, the airflow is 1/6 of the distorted compressor airflow. According to it, if the high pressure region constitutes $300^o/360^o = 5/6$, the airflow through this compressor would be 5/6 of the distorted compressor airflow. Figure 13 shows the distortion pattern of the example and represents both compressors working in parallel.

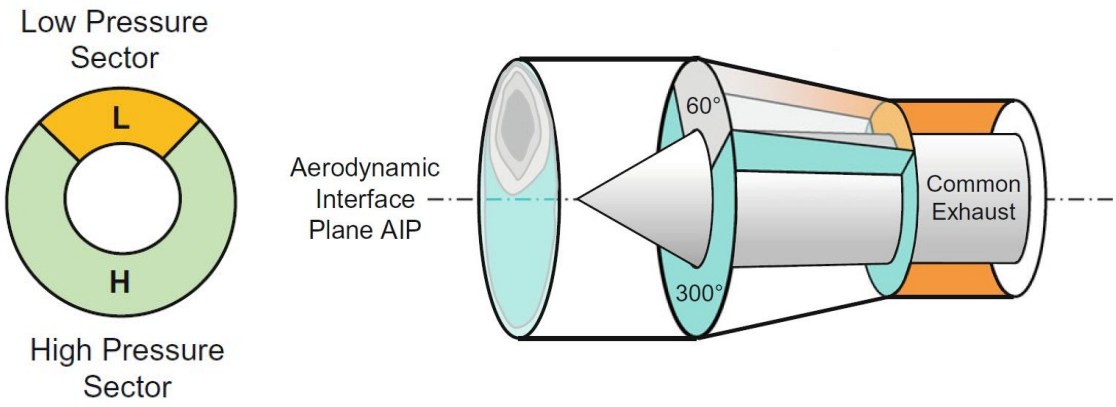

(a) Distortion pattern (b) Two compressors working in parallel

Figure 13: Scheme of parallel compressor model. Reproduced from Kurzke [5].

In figure 14 an example of a compressor map is represented in order to analyse qualitatively the response of the compressor against different types of distortion. Clean operation points (M) are represented with its clean surge line. The compressor with lower pressure (L) operates with a higher pressure ratio, while the compressor with higher pressure (H) operates with lower pressure ratio. When distortion increases, both operation points move away from each other to keep the same static pressure at the compressor outlet, until the low pressure operation point reaches the clean surge line, moment in which the instability is considered to appear.

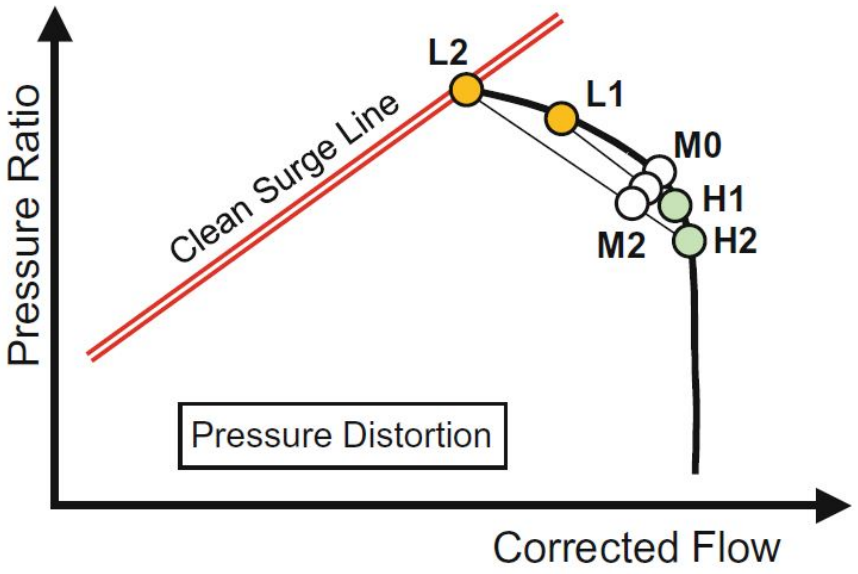

Figure 14: Compressor map with operating points of high and low pressure compressors. Reproduced from Kurzke [5].

As pressure ratio of low pressure compressor is too high, surge appears in the compressor even the operation point is not close to the clean surge line. In the figure of the compressor map, the operation point in which surge occurs is M2 and it is calculated with the weighted average between the operating points of both compressors.

Some references, such as Longley [27], Kurzke [13] or Pokhrel [6], indicate there is a critical sector angle above which the pressure ratio for which surge is produced does not decrease. It is shown in figure 15, where a critical angle of $\theta = 90^o$ is defined. It has also been proven that, as the corrected speed increases, the pressure ratio in which the surge occurs decreases.

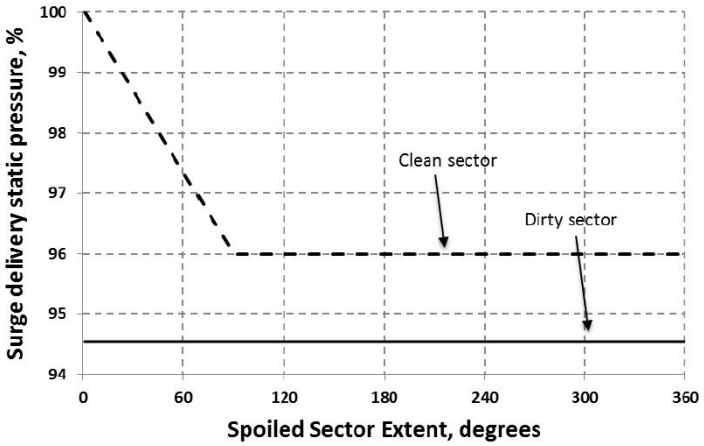

Figure 15: Experimental and numerical results showing critical angle $\theta = 90^o$. Reproduced from Pokhrel et al. [6]

In summary, the operating point of the distorted compressor can be calculated using the parallel compressor model. This technique is widely used experimentally and it can be used numerically with an analytical model that simulates the behavior of an engine against distortion.

3.2 PCM implementation in MATLAB

As it has been shown before, when pressure distortion appears on the AIP, the behaviour of the compressor changes. An analytical model has been implemented in MATLAB, applied to the low pressure compressor map of Larzac04 engine and validated with experimental results from Larzac04 [7] and PW-1128 [28] engines.

Figure 16 shows the LPC map with the steady state line (black line), which are the points through which the engine typically passes during operation. The map also shows the clear surge line (red line), which represents the pressure ratio for which surge will appear for a given value of corrected engine airflow and without distortion.

Some corrected speed lines (blue lines) are also represented for values between 73% and 100% of design corrected speed. Conditions before the compressor are noted with subscript “2”, while conditions after the compressor are noted with subscript “3”.

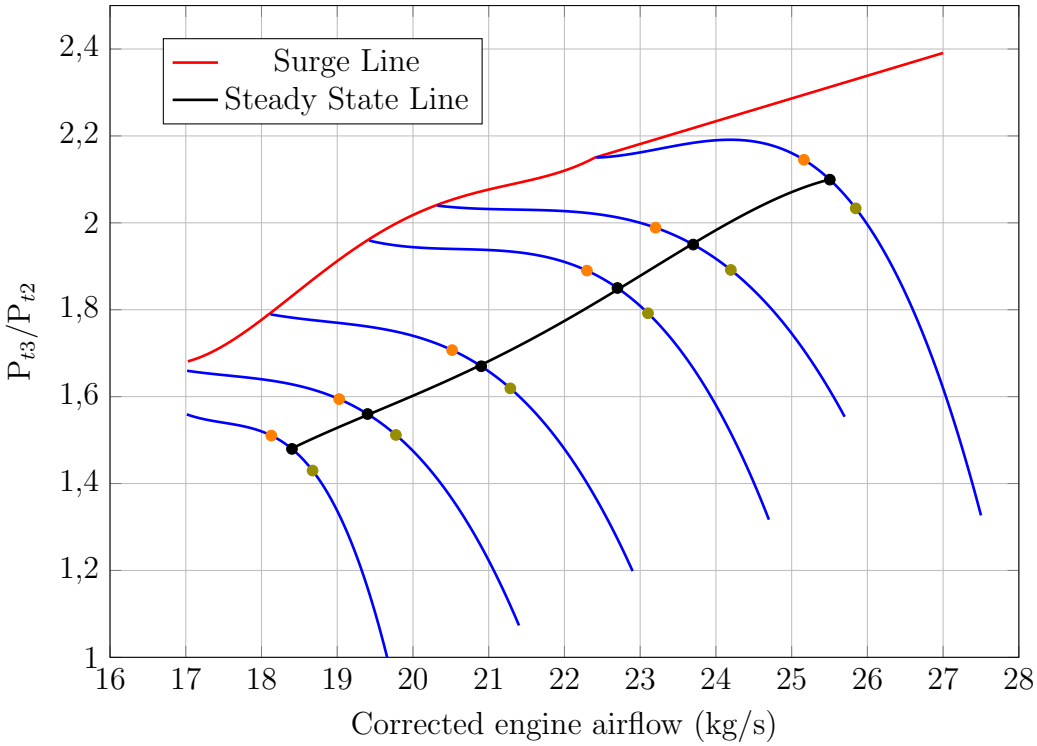

Figure 16: LPC map of Larzac04 engine.

Once these lines are defined, when a distorted flow enters through the compressor, the parallel compressor model is applied to the points of the steady state line. This distortion leads two operation points, one for each region with different values of static pressure at the compressor discharge ($P_{3,S}$). This value is studied for several pairs of points, increasingly separated from each other; until a pair whose $P_{3,S}$ values match is found. Both points are represented for each corrected speed line, the orange one refers to the low pressure region while the green one refers to the high pressure region.

$\dot{m}_{corr}$	Corrected engine airflow	P_{t3}/P_{t2}	Pressure ratio
P_0	Ambient pressure	T_0	Ambient temperature
M	Mach number	A	Compressor area
CDI_{mean}	Circular distortion index	β	Spoiled angle
RR	Ram Recovery	η_{is}	Isentropic efficiency

Table 7: Initial values needed to calculate the operating point with distortion

The process to calculate the static pressure at the compressor discharge needs some values related with compressor operation conditions, ambient conditions, characteristics of the distortion and characteristics of the engine. These values are shown in table 7. This process is as follows:

Flows with circumferential distortion characterized by CDI_{mean} can be modeled as a pressure map with two regions. The high pressure region has the same value ($P_{t2,High}$) as the one that had the AIP operating without distortion. The pressure of the distorted region depends on the intensity of distortion (CDI_{mean}) and its extent β:

$$P_{t2,LP} = \frac{1-\beta}{\frac{1}{1-CDI_{mean}} - \beta} P_{t2,HP} \tag{8}$$

On the one hand, real engine airflow is calculated:

$$\dot{m}_{real} = \dot{m}_{corr} \frac{P_{t2}}{P_{ISA}} \sqrt{\frac{T_{ISA}}{T_{t2}}} \tag{9}$$

The engine airflow which passes trough each compressor is calculated with the spoiled angle:

$$\dot{m}_{real,LP} = \beta \dot{m}_{real} \tag{10a}$$
$$\dot{m}_{real,HP} = (1-\beta) \dot{m}_{real} \tag{10b}$$

On the other side, P_{t2} is obtained with the values of ambient pressure P_0, Mach number and Ram Recovery. P_{t3} is calculated with it and the pressure ratio:

$$P_{t0} = P_0 \left(1 + \frac{\gamma - 1}{2} M^2\right)^{\frac{\gamma-1}{\gamma}} \tag{11a}$$
$$P_{t2} = P_{t0} RR \tag{11b}$$
$$P_{t3} = \pi_{2,3} P_{t2} \tag{11c}$$

Finally, temperature T_{t2} depends on atmospheric temperature and Mach number. Since pressure ratio is known for each point of the map, an isentropic evolution of the compressor can be assumed to, known its isentropic efficiency, determine the temperature ratio throughout it. With this temperature ratio, T_{t3} is calculated:

$$T_{t2} = T_{t0} = T_0 \left(1 + \frac{\gamma - 1}{2} M^2\right) \tag{12a}$$
$$\frac{T_{t3}}{T_{t2}} = 1 + \frac{\pi_{2,3}^{\frac{\gamma-1}{\gamma}} - 1}{\eta_{is}} \tag{12b}$$

Once m_{real}, T_{t3} and P_{t3} are calculated, static pressure at compressor discharge is determined from Mach number which was obtained using the relation:

$$\frac{\dot{m}\sqrt{\gamma R T_{t3}}}{\gamma P_{t3} A} = \frac{M}{\left[1 + \left(\frac{\gamma-1}{2}\right) M^2\right]^{(\gamma+1)/2(\gamma-1)}} = \frac{M}{(1 + 0.2M^2)^3} \tag{13}$$

With the Mach at compressor discharge and P_{t3}, static pressure is calculated:

$$P_{3,S} = \frac{P_{t3}}{\left(1 + \frac{\gamma-1}{2}M^2\right)^{\frac{\gamma-1}{\gamma}}} \tag{14}$$

This process is done with both high and low pressure points and its values of static are compared. While these values are different, both points move away each other until a pair of points have the same static pressure $P_{3,S}$ at compressor discharge.

When a distorted flow enters through the compressor, the surge line moves closer to the steady state line. It is possible to calculate the modified surge line as a function of the distortion by imposing that the low pressure point is on the clear surge line and looking for the high pressure point with the same static pressure $P_{3,S}$.

With both points, the original point which produces the situation imposed with the defined distortion is the point for which surge will appear. Surge margin is defined by taking in count the difference in pressure ratio between the steady state line (SSL) and the surge line (SL) which is in the vertical of the first:

$$SM(\%) = \frac{PR_{SL} - PR_{SSL}}{PR_{SSL}}\ 100\ \% \tag{15}$$

3.3 Application case: Larzac04 Low Pressure Compressor

3.3.1 Validation of Larzac04 LPC

Parallel compressor model described above has been applied to the low pressure compressor of Larzac04 engine. First, analytical results obtained with the proposed model have been compared with experimental results obtained by Rademakers et al. in reference [7], where the influence of S-Duct inlets on the performance and stability of a jet engine has been studied. Using some screens as distortion generator, surge margin of the compressor was related with the mean circular distortion index. The model has been applied to the points of the steady state with the next conditions:

- Altitude → h = 11.000 m → P_0 = 22.600 Pa and T_0 = 216.6 K
- Mach → M = 0.8 → P_{t0} = 34.500 Pa and T_{t0} = 244.4 K
- Ram Recovery → RR = 0.99 → P_{t2} = 33.800 Pa
- Isentropic efficiency → $\eta_{is} = 0.8$
- Spoiled angle → $\beta = 90^o/360^o = 1/4$
- Inlet area → A = 0.16 m^2

Ram recovery of 0.99 has been chosen, a typical value for inlets nowadays. About isentropic efficiency of the compressor, η_{is} = 80 % has been chosen as a typical value of low pressure compressors in the absence of information regarding this compressor property. The spoiled angle chosen was 90^o, which is the critical angle above which there is hardly any variation in new surge point obtained.

After applying the analytical model to the compressor experimentally tested, the analytical results follow the same trend as those obtained through tests, which are shown in figure 17. Even analytical results fit very well the experimental points, this model should be used carefully, because some points are below the analytical line. It could lead to calculate analytically a value of surge margin which is higher than the real value, being dangerous for high CDI values that are close to surge.

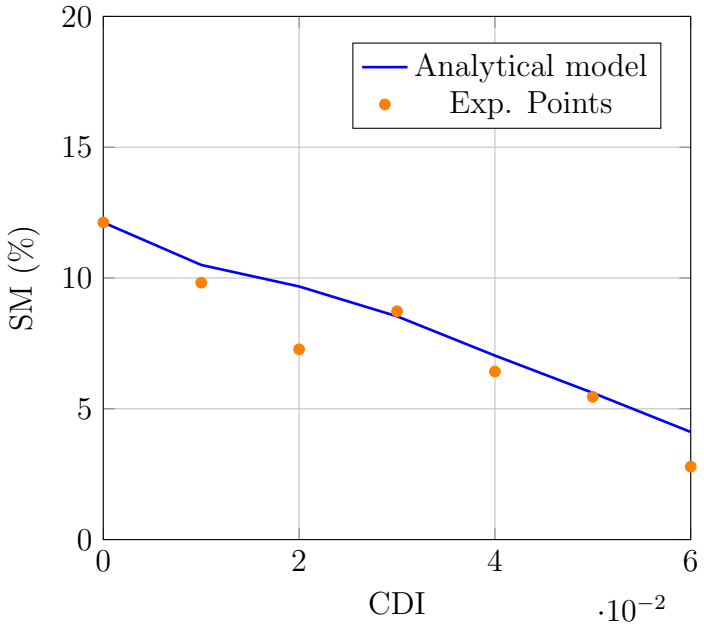

Figure 17: Comparison between analytical results calculated and experimental results from reference [7].

These results are also shown in table 8, where the value of surge margin for both analytical and experimental results is presented.

CDI	0	0.01	0.02	0.03	0.04	0.05	0.06
Analytical results	12.1 %	10.5 %	9.7 %	8.5 %	7.0 %	5.6 %	4.1 %
Experimental results	12.1 %	9.8 %	7.3 %	8.7 %	6.4 %	5.5 %	2.8 %
Error	0 %	0.7 %	1.4 %	0.2 %	0.6 %	0.1 %	1.3 %

Table 8: Surge margin variation for different values of Circumferential distortion index.

However, the error obtained is small and it has also been considered that, due to the complexity of the problem and the simplicity of the proposed analytical model, the results obtained are good enough to estimate the behavior of a compressor against pressure distortions.

3.3.2 Results of Larzac04 LPC

The evolution of the stability margin with the corrected speed is calculated for different values of circular distortion. Circular distortion index has been used to evaluate the evolution of the surge margin for different operation points.

To obtain the evolution of the surge margin with the circular distortion index, some values between $CDI_{mean} = 0$ (clean section) and $CDI_{mean} = 6$ % have been chosen. Values of corrected engine airflow and pressure ration are different for each operation point. These pairs of values are shown in table 9.

Point	**1**	**2**	**3**	**4**	**5**	**6**
Pressure ratio	1.48	1.56	1.67	1.85	1.95	2.10
Corr. eng. airflow (kg/s)	18.4	19.4	20.9	22.7	23.7	25.5

Table 9: Pressure ratio and corrected engine airflow of operating points in figure 16

When distortion index increases, surge line moves in the low pressure compressor map, approaching the steady state line. It means that for higher values of CDI, surge margin will decrease. Figure 18 shows the compressor map of Larzac04 with the surge line and its position for different values of circular distortion.

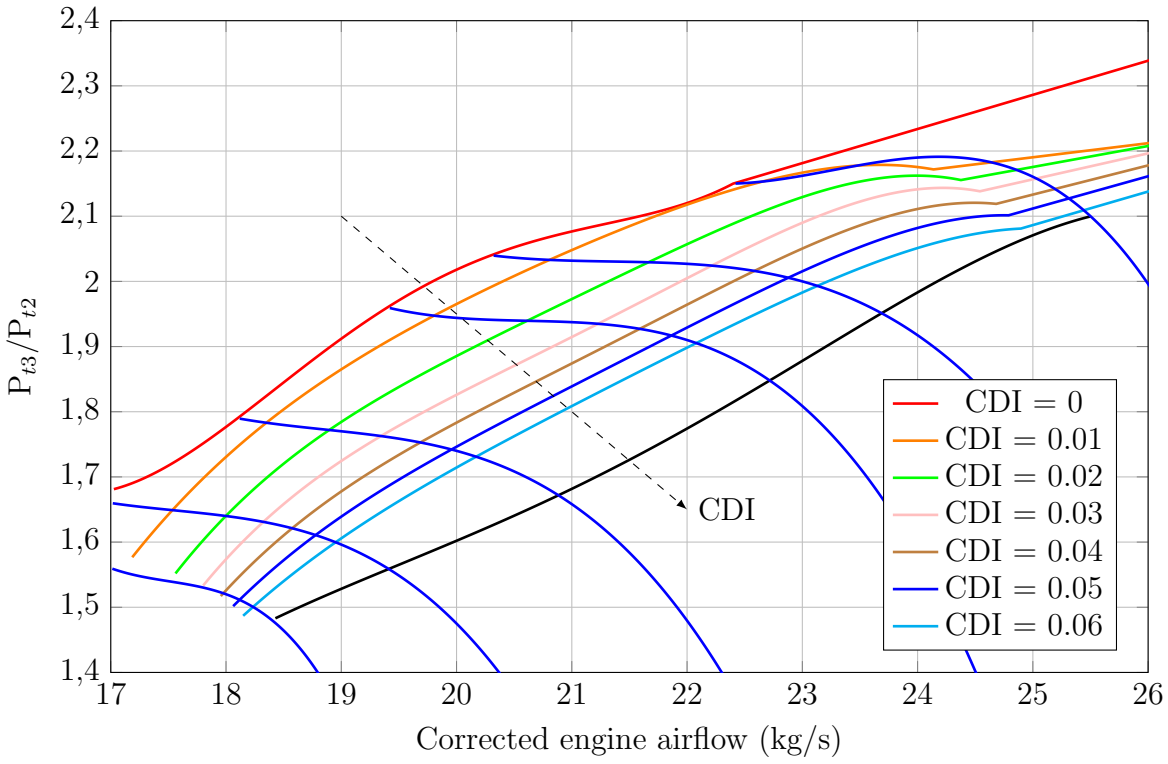

Figure 18: LPC map of Larzac04 engine with the calculated surge line for different values of CDI.

Surge margin of operation points decreases when corrected speed increases, which is shown in figure 19. It happens because, when the operation point is moving through the steady state line from lower to higher corrected speeds, both turbine inlet temperature and corrected engine airflow increase, so pressure ratio of the compressor also increases, moving away from turbine chocking conditions and approaching the surge line.

For low corrected speed values, the compressor can operate with larger distortions without getting too close to the surge line, but when corrected speed increases and it approaches 100 % of its design value, distortion is more dangerous and smaller distortions can lead to surge.

In the studied compressor, for CDI = 6 %, it operates with SM = 0.07 at 80 % of corrected speed, while the same distortion drives to a SM = 0.01 at 100 % of corrected speed.

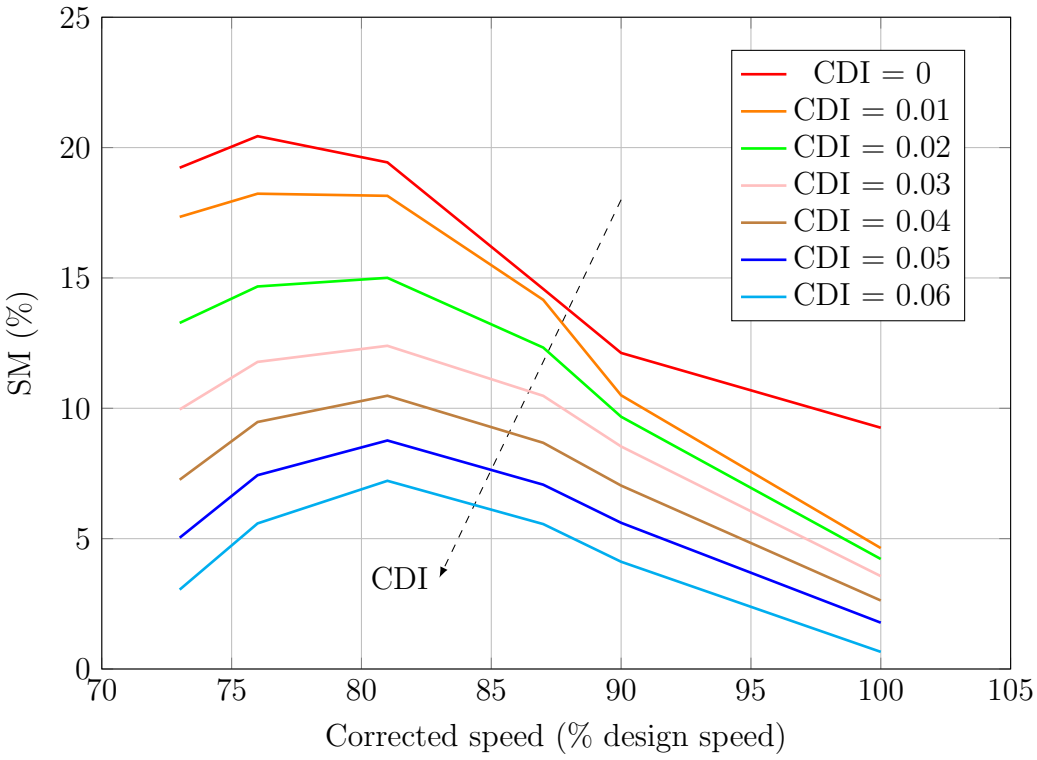

Figure 19: Surge margin evolution with corrected speed for different CDI.

As it was explained before, surge margin decreases when distortion increases. Figure 20 shows the evolution of surge margin with CDI for different values of corrected speed N_C. The bigger the distortion in the flow is, the higher the value of circular distortion index and the lower the surge margin.

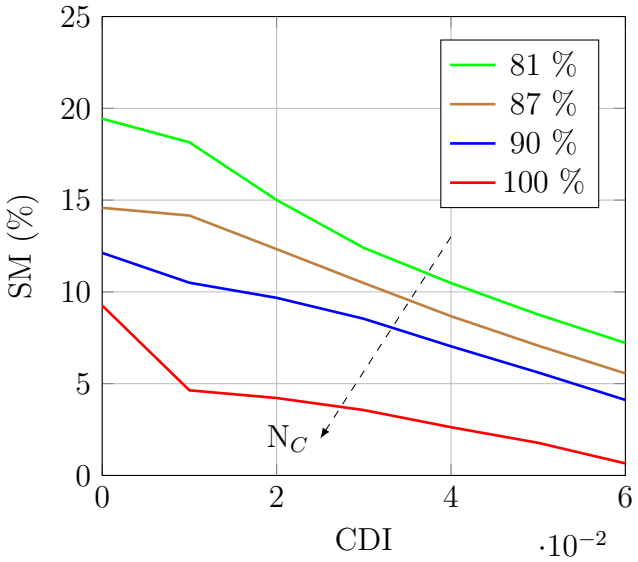

Figure 20: Surge margin evolution with circular distortion index for different corrected speeds.

This tool is also useful to analyse the inlet/engine distortion compatibility, which is the behaviour of the compressor for different manoeuvres and flight conditions. CFD tools or experimental tests can be used to study the evolution of the flow through the inlet and to define the pressure distribution in the aerodynamic interface plane.

	CDI_{mean} (%)	**SM (%) N_C=80%**	**SM (%) N_C=90%**	**SM (%) N_C=100%**
Ex. 1	1.70	17.2	10.1	4.5
Ex. 2	2.95	12.8	8.3	3.8
Ex. 3	0.52	10.2	11.5	7.3
Ex. 4	0.35	19.4	11.8	7.5

Table 10: Values of CDI_{mean} and surge margin for the examples of figure 7 with LPC of Larzac04.

Examples presented in figure 7 are used to estimate the surge margin. Results obtained are presented in table 10. Since distortion is more dangerous when the corrected speed increases, surge margin values obtained for $N_C = 80\%$ are high and the pressure maps presented before will not entail any danger to the operation of the engine.

When corrected speed increases to $N_C = 90$ %, example 2 presents a surge margin value of 8.3 %, which means that is possible to operate with this distortion but the surge point is not too far. If corrected speed is $N_C = 100$ %, all examples operate with surge margin around 5 %. Moreover, example 2 is the most critical case with a surge margin of 3.8 %. This is a low value, which means that the surge point is close and small perturbations that increase the pressure ratio can lead to surge.

Hence, combinations of manoeuvres and flight conditions that lead to high values of circular distortion index are not a problem for small corrected speeds; but when corrected speed increases, a pressure distribution that was previously acceptable can now lead to surge.

3.4 Application case: PW-1128 Low Pressure Compressor

3.4.1 Validation of PW-1128 LPC

A second validation is done to confirm that the model presented above provides accurate results. In this case, analytical results obtained after applying the parallel compressor model to the low pressure compressor of PW-1128 engine are compared with the experimental results obtained by Mehalic [28].The model has been applied to the points of the steady state with the next conditions:

- Altitude $\rightarrow$ h = 30.000 ft = 9144 m $\rightarrow$ P_0 = 30.088 Pa and T_0 = 228.7 K
- Mach $\rightarrow$ M = 0.8 $\rightarrow$ P_{T0} = 45.854 Pa and T_{T0} = 258 K
- Ram Recovery $\rightarrow$ RR = 0.99 $\rightarrow$ P_{T2} = 45.406 Pa
- Isentropic efficiency $\rightarrow$ $\eta_{is} = 0.8$
- Spoiled angle $\rightarrow$ $\beta = 90^{o}/360^{o} = 1/4$

Ram recovery chosen was 0.99, a typical value for inlets nowadays. About isentropic efficiency of the compressor, $\eta_{is} = 80$ % has been chosen as a typical value of low pressure compressors

in the absence of information regarding this compressor property. Spoiled angle chosen was 90^{o}, which is the critical angle above which there is hardly any variation in new surge point obtained.

In the reference from which experimental results have been taken, results are presented as a compressor map with the experimental surge line obtained for different values of circular distortion indexes depending on the corrected speed line. Figure 21 shows the results obtained experimentally and also the surge line calculated with the implemented model.

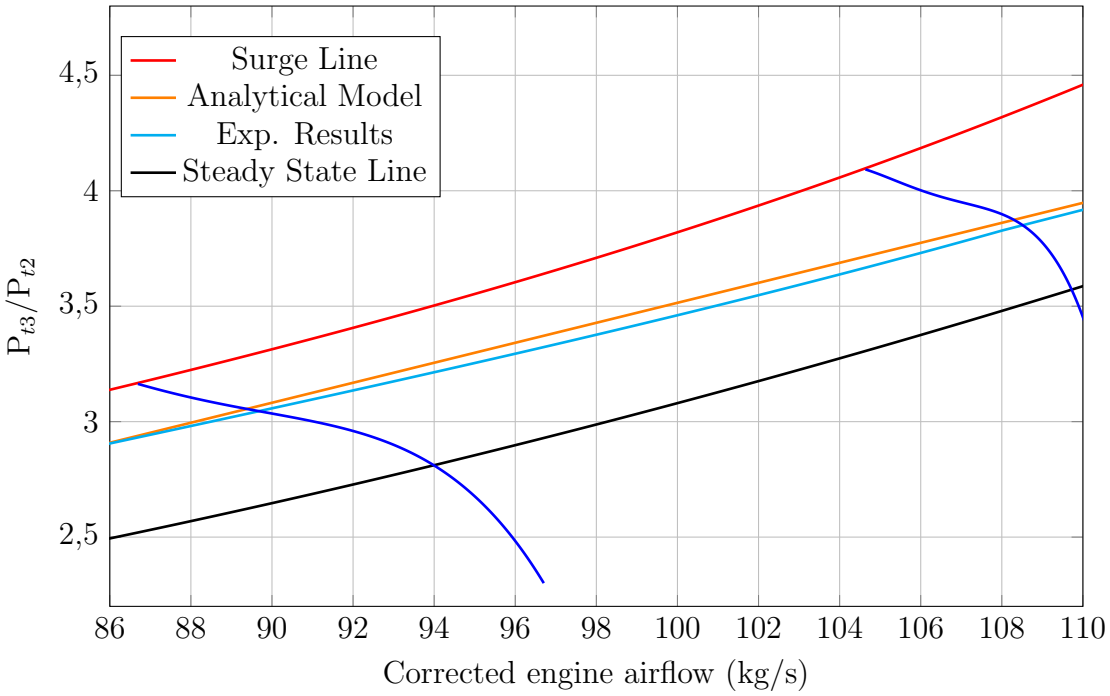

Figure 21: LPC map of PW-1128 engine with the experimental surge line and the calculated one with the model proposed.

Results given by the analytical model and those given by the the experimental one are close as it is shown in table 11. ΔPRS is the percent loss of surge pressure ratio of the distorted surge line regarding the clean surge line. This value has been calculated for the analytical surge line and the experimental one.

The difference in ΔPRS is between 0.9 % and 1.5 %, which agrees with results obtained by Kurzke [5], where differences around 2 % where obtained. It leads to conclude that the implemented model is enough accurate to estimate the behaviour of the compressor under compressor distortion.

	Nc = 90 %		Nc = 92.5 %		Nc = 95 %		Nc = 97.5 %		Nc = 100 %	
	PR	ΔPRS	PR	ΔPRS	PR	ΔPRS	PR	ΔPRS	PR	ΔPRS
Clean SL	3.50	-	3.71	-	3.96	-	4.17	-	4.43	-
An. SL	3.26	6.9 %	3.43	7.5 %	3.63	8.3 %	3.77	9.6 %	3.94	11.1 %
Exp. SL	3.21	8.3 %	3.38	8.9 %	3.57	9.8 %	3.72	10.8 %	3.90	12 %
Error	1.4 %		1.4 %		1.5 %		1.2 %		0.9 %	

Table 11: Pressure ratio variation from clean surge line to distorted surge line.

Surge margin of both cases has been calculated. Figure 22 shows the evolution of the surge margin with the corrected speed calculated analytically. Also, some experimental points obtained by Mehalic [28] are represented.

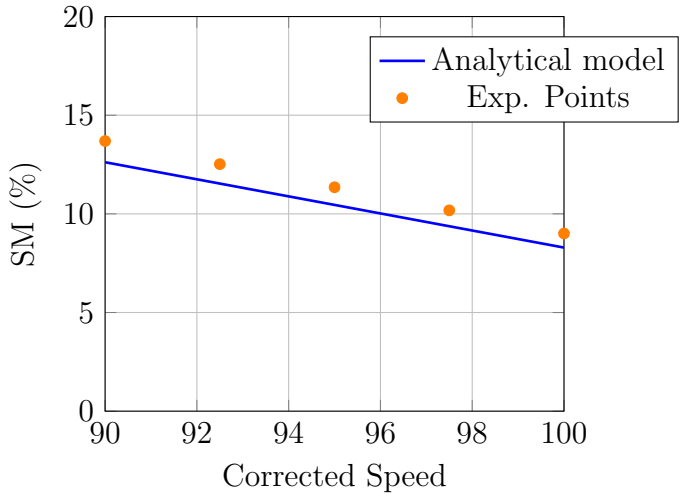

Figure 22: Surge margin obtained experimentally compared with results calculated with the analytical model.

3.4.2 Results of PW-1128 LPC

After validating the applied model also with the low pressure compressor of PW-1128, some results have been calculated in order to show the evolution of the surge margin for different circular distortion indexes and different corrected speeds. Three points from the steady state line have been used to calculate the surge margin for three corrected speeds. These pairs of pressure ratio and corrected engine airflow are shown in table 12.

Point	**1**	**2**	**3**
Pressure ratio	2.18	2.81	3.58
Corr. eng. airflow (kg/s)	76.5	94.0	109.7

Table 12: Pressure ratio and corrected engine airflow of operating points in figure 23

Due to the influence of distortion, surge line approaches steady state line when distortion increases. Some values between $CDI_{mean} = 0$ (clean section) and $CDI_{mean} = 12$ % have been chosen to calculate the variation of the surge line with CDI.

Figure 23 shows the clean surge line in red, for which CDI = 0 and other lines that represent different values of CDI. Black line is the steady state line and is the line from which the points of the table 12 have been taken.

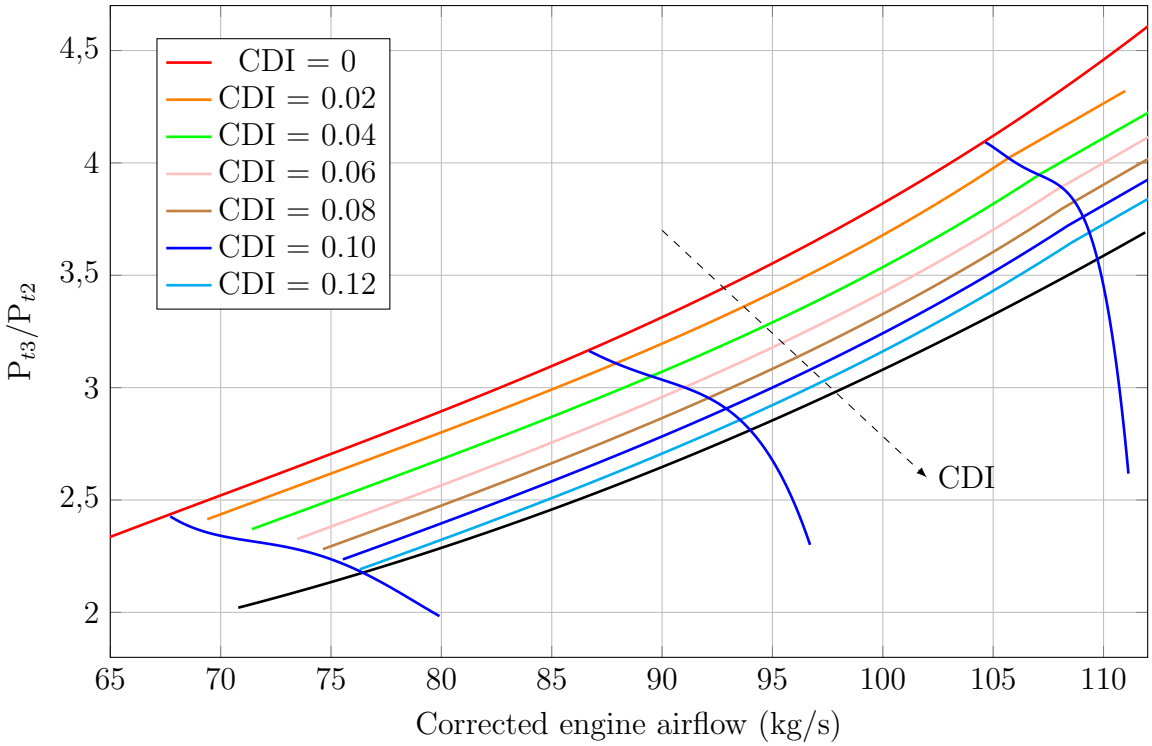

Figure 23: LPC map of PW-1128 engine with the calculated surge line for different values of CDI.

The new surge lines obtained allow to calculate the surge margin for different CDI. The previous map shows three corrected speed lines, which refer to 80 %, 90.1 % and 100.2 % of corrected speed. Surge margin for each of these lines and CDI shown before has been calculated, which is shown in figure 24.

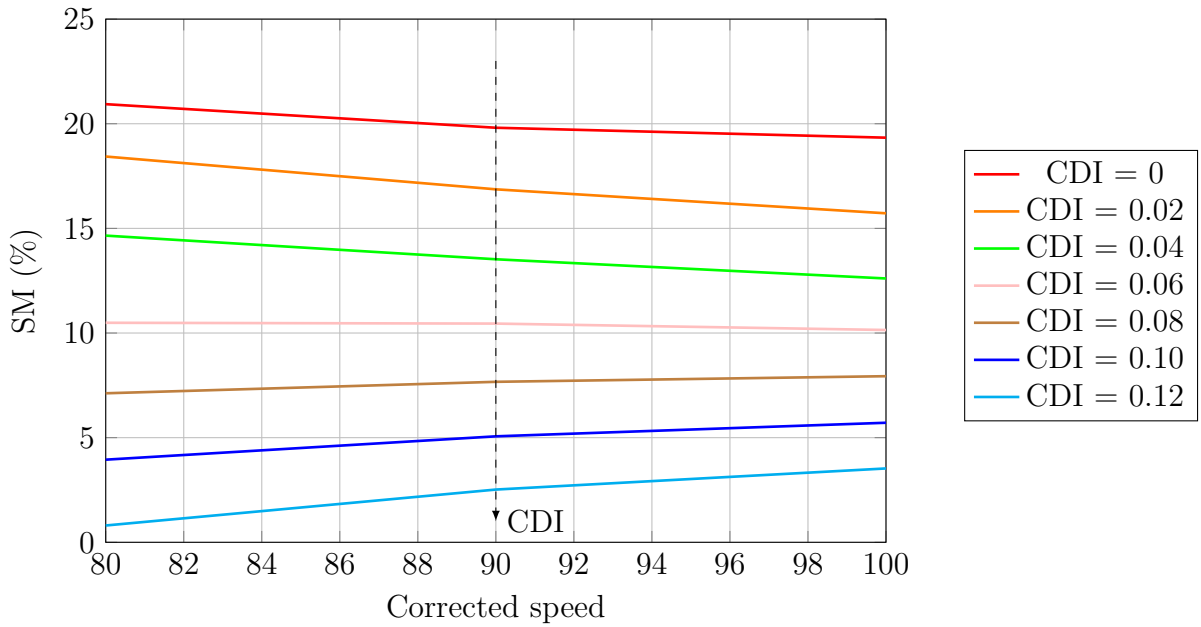

Figure 24: Surge margin evolution with corrected speed for different CDI.

In this case, surge margin decreases with corrected speed only for low values of circular distortion indexes, while it increases with corrected speed for high values of CDI. It is also possible to see

that there are clear differences between the surge margin obtained for each value of distortion, decreasing the surge margin and approaching the surge line when distortion increases. Figure 25 shows it.

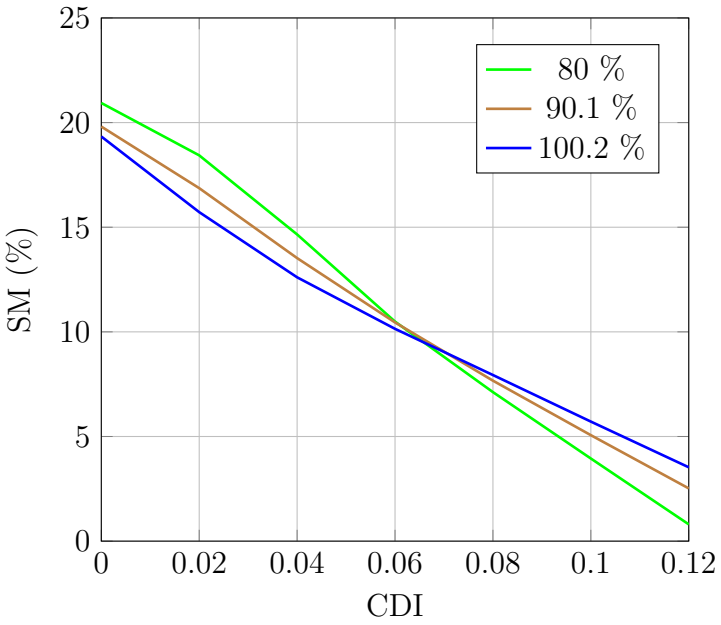

Figure 25: Surge margin evolution with circular distortion index for different corrected speeds.

The slope of these three lines has been computed with the aim of comparing the influence of the speed lines on sensitivity to surge. Reference value of 100 % of slope has been given to the corrected speed line N_C = 80 % because it is the highest one. Table 13 shows the values obtained for the three speed lines computed.

N_C	80 %	90.1 %	100.2 %
Slope	100 %	86 %	78 %

Table 13: Slope of SM vs CDI evolution for different corrected speeds

Results from figure 25 and table 13 show that when corrected speed increases, slope of the line that relates surge margin with circular distortion index decreases. For example, if CDI is zero, for corrected speed of N_C = 80 % surge margin is 21 %; whilst for N_C = 100 % surge margin is 19 %. When CDI = 0.06, both corrected speeds have a surge margin of 10 %. Otherwise, when CDI = 0.12 and both results are close to surge, for N_C = 80 % surge margin is 1.5 %; whilst for N_C = 100 % surge margin is 4 %.

This is consistent with the expected behavior of the air-breathing engines against surge, because they are designed to tolerate surge better for higher corrected speeds, which are closer to the most typical during engine operation.

As it was explained before, the compatibility between nacelle and compressor can be studied with this tool. Since different nacelles will provide different maps of pressures at the aerodynamic interface plane, these maps can be studied and its circular distortion index can be calculated. Once CDI is computed, it is possible to estimate the new surge line on the compressor map, which allow to calculate the new surge margin.

In the same way as in the previous section, examples shown in the figure 7 are used to calculate the surge margin for different corrected speeds. Results are presented in table 14.

	CDI_{mean} (%)	**SM (%) N_C=80%**	**SM (%) N_C=90%**	**SM (%) N_C=100%**
Ex. 1	1.70	15.5	14.4	13.6
Ex. 2	2.95	12.2	11.9	11.6
Ex. 3	0.52	17.6	16.5	15.7
Ex. 4	0.35	18.0	16.9	16.1

Table 14: Values of CDI_{mean} and surge margin for the examples of figure 7 with LPC of PW-1128.

Because distortion values are between 0.35 % and 2.95 %, surge margin calculated is high (11.6 % in the worst case, when CDI_{mean} = 2.95 % and N_C=100%) so operation with this distortion indexes is not dangerous for the engine.

4 Swirl Distortion - Effect on compressor stability

Swirl distortion can be defined as the presence of axial velocity at the Aerodynamic Interface Plane. Its main effect is the change on the incidence angle between the flow and compressor blades, which will lead to changes on the loading of the blade, which is associated with a modification in the operating point.

When distortion started to be studied, pressure distortion monopolized all the effort of engineers because it was the most common type of distortion. Swirl distortion has been coupled with pressure distortion and it has not been studied separately until last years, where ultra-high bypass ratio engines have been developed, at the same time that turboprops and military airplanes whose engines are embedded in the fuselage.

Some examples of these configurations are shown in figure 26. The first one is the General Electric engine GE90 (reproduced from GE Aviation [29]), used nowadays in long-range aircrafts as Boeing-777. The second one is Europrop TP400 (reproduced from MTU Aero Engines [30]), used on A400M of Airbus, a transport military aircraft. The third example is Tornado fighter aircraft (reproduced from Airbus [31]), one of the first examples where swirl distortion was important by itself.

(a) GE90 [29] (b) TP400 [30] (c) Tornado [31]

Figure 26: Engines and aircraft susceptible to ingest swirl distortions

These new configurations had as a consequence higher swirl distortions than in older configurations. For example, S-shaped intake of Tornado fighter aircraft produced a high amount of counter-rotating swirl which produced instabilities before predicted only taking in count pressure distortion. Therefore, swirl distortion started to be studied decoupled from pressure distortion.

New designs of aircraft are based on join both engine and fuselage. This involves important problems in terms of air-intake and engine compatibility due to the apparition of swirl distortion caused by complex air-intake shapes so, right now, swirl distortion is an interesting topic which is studied by many companies and research centers.

4.1 Types of swirl distortion

Swirl distortion can be defined with the swirl angle α, which is the angle between the axial velocity and the circumferential velocity. Depending on the distribution of the swirl angle in

the AIP, some types of swirl distortion can be defined.

- Bulk swirl: The entire flow presents the same swirl angle. If the axial velocity rotates as the compressor does, it is called co-rotating bulk swirl and $\alpha > 0$. If the axial velocity is opposite to the compressor velocity, it is called counter-rotating bulk swirl and $\alpha < 0$. This swirl pattern is illustrated in figure 27.

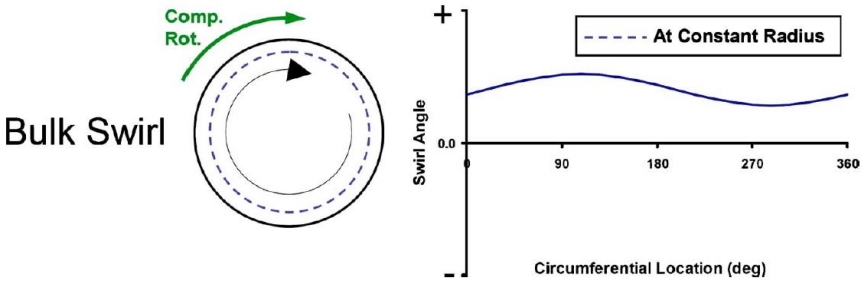

Figure 27: Typical bulk swirl pattern. Reproduced from Sheroan et al. [8].

- Paired swirl: It is the most common type of swirl, which is produced typically by S-shaped ducts or plenum style intakes used in APUs. It consist in two vortices of opposite direction which magnitudes can be equal or different. If both vortices have the same magnitude, it is referred as twin swirl, but if the magnitudes are different, it is called offset swirl. Figure 28 shows both types of paired swirl.

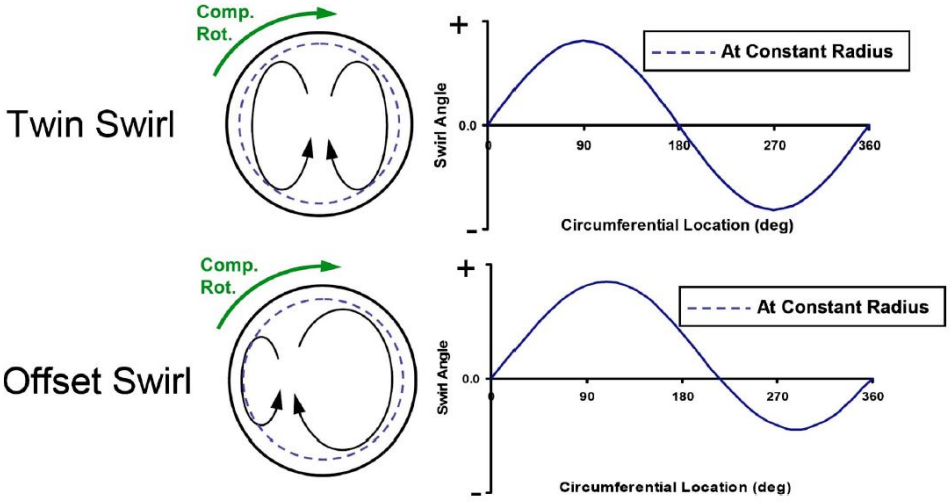

Figure 28: Two types of typical paired swirl patterns. Reproduced from Sheroan et al. [8].

- Tightly wound vortices: These distortions are produced by the ingestion of ground vortices during operation or due to the use of S-shaped intakes. Its size, location and intensity depend on different factors, so a wide variety of tightly wound vortices can appear. Figure 29 shows examples of tightly wound vortices formation.

  There are usually three key necessary elements to create this kind of vortices: a flow sink, a stagnation point, and a source of vorticity in the surrounding flow field [10]. Since any of them can appear, change or disappear over time; these vortices have a strong unsteady component.

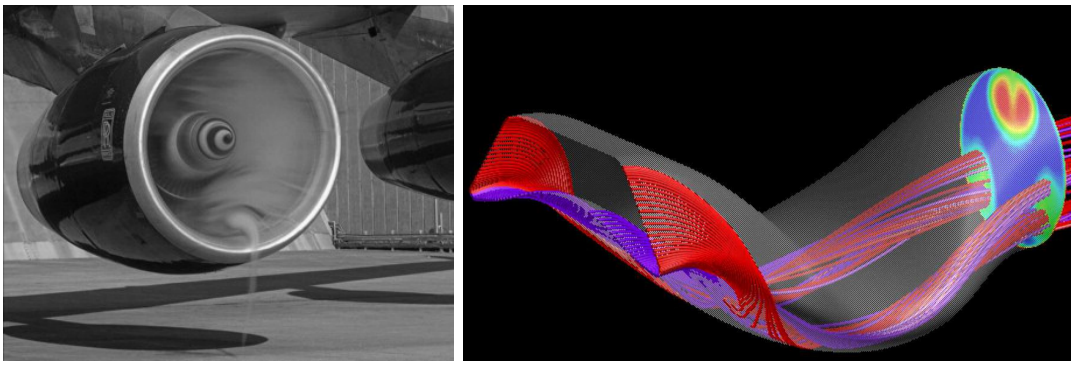

(a) Ground vortex ingestion (b) S-shaped vortex formation

Figure 29: Typical methods of tightly wound vortices formation. Reproduced from Murphy et al. [9] and Mehdi [10] respectively.

4.2 Description of swirl distortion

There are different patterns of swirl distortion. One or more than one vortices, with equal or different intensities, some of then rotating in the same direction than the compressor and others rotating in the opposite direction, etc. This wide variety makes it necessary to define some parameters to describe the characteristics of each swirl distortion pattern.

Following the previous research done by the Society of Automotive Engines (SAE) in terms of pressure distortion, some descriptors have been developed by the S16 Turbine Engine Inlet Distortion Committee, [11]. These descriptors have not been yet consolidated, but have been used by several authors as Mehdi [10] or Sheoran [8] and are well accepted among the engineers working on this topic.

Three descriptors have been developed based on the distribution of swirl angle in the AIP: Swirl intensity (SI), swirl directivity (SD) and swirl pair (SP). Two sub-parameters are calculated for first to obtain these descriptors: extent (θ_i^+, θ_i^-) and sector swirls (SS_i^+, SS_i^-).

4.2.1 Sub-parameters

In the same way it has been done previously with pressure distortion, the aerodynamic interface plane should be divided in rings and sectors. These sub-parameters are going to be calculated for each ring.

- Extents (θ_i): It is the size of the region where swirl angle is positive (θ_i^+) or negative (θ_i^-), meaning that flow is co-rotating or counter-rotating compared to the compressor respectively. According with figure 30, extents can be calculated with equations 16.

$$\theta_i^+ = \theta_{2i} - \theta_{1i} \tag{16a}$$

$$\theta_i^- = \theta_{3i} - \theta_{2i} \tag{16b}$$

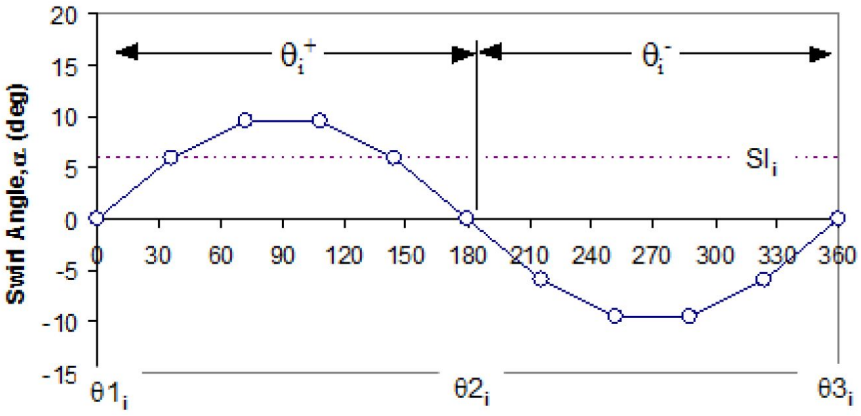

Figure 30: Typical symmetric paired swirl pattern. Reproduced from SAE [11].

- Sector Swirls (SS_i): Quantify the swirl sector by integrating the distribution of the swirl angle α for each ring. SS_i^+ refers to the co-rotating region while SS_i^- is related with the counter-rotating region.

$$SS_i^+ = \frac{1}{\theta_i^+} \int_{\theta_i^+} \alpha(\theta)_i \, d\theta \tag{17a}$$

$$SS_i^- = \frac{1}{\theta_i^-} \int_{\theta_i^-} \alpha(\theta)_i \, d\theta \tag{17b}$$

4.2.2 Descriptors

- Swirl Intensity (SI): It represents the absolute magnitude of the swirl angle in each ring. It can be calculated with equation 18.

$$SI_i = \frac{SS_i^+ \theta_i^+ + |SS_i^-| \theta_i^-}{360} \tag{18}$$

- Swirl Directivity (SD): It represents the rotational direction between the flow and the compressor. In the case of pure co-rotating bulk swirl, SD will be 1, while if the swirl pattern is pure counter-rotating, SD will be -1. Equation 33 shows how to calculate it and figure 31 represents the possible values that swirl directivity can reach depending on the swirl pattern.

$$SD_i = \frac{SS_i^+ \theta_i^+ + SS_i^- \theta_i^-}{SS_i^+ \theta_i^+ + |SS_i^-| \theta_i^-} \tag{19}$$

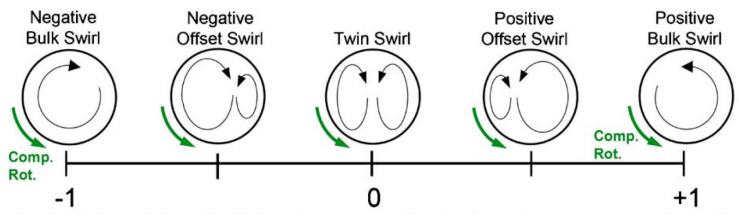

Figure 31: Possible values of swirl directivity. Reproduced from SAE [11].

- Swirl Pair: It represents the number of alternating swirl pars which are present in each ring. The minimum value of SP is 0.5, obtained when there is pure bulk swirl (co-rotating or counter-rotating). In the opposite case, SP is 1 when there is a paired swirl where both regions have the same extent (twin swirl). Figure 32 shows the spectrum of values that can be reached by swirl pair. It can be calculated with equation 20.

$$SD_i = \frac{SS_i^+\theta_i^+ + |SS_i^-|\theta_i^-}{2\max[(SS_i^+\theta_i^+), (|SS_i^-|\theta_i^-)]} \tag{20}$$

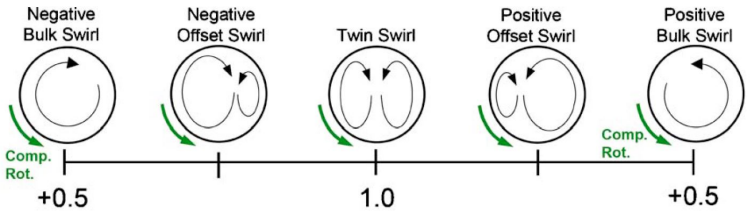

Figure 32: Possible values of swirl pair. Reproduced from SAE [11].

4.3 Interaction between fluid and compressor blades

When the fluid reaches the compressor, its velocity can be decomposed into its absolute and relative components which, together with the rotational speed of the rotor, build the velocity triangle. Figure 33 shows this evolution through the blade of the rotor.

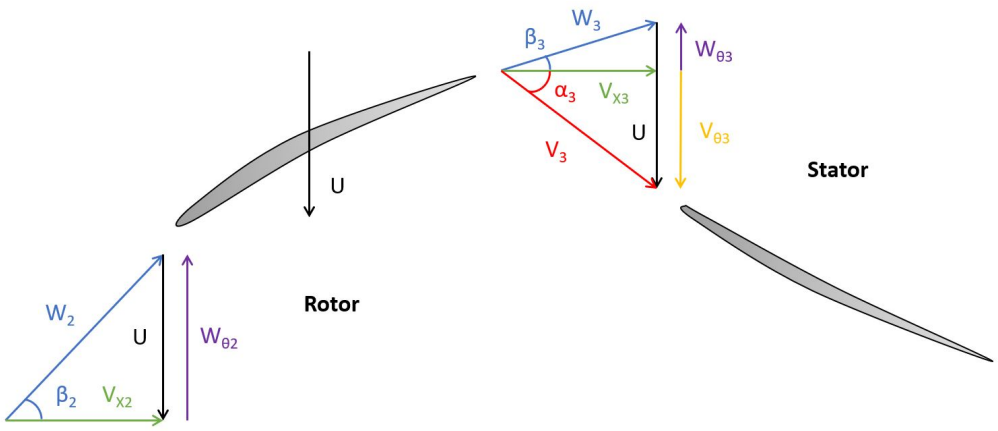

Figure 33: Velocity triangles before and after a rotor blade.

Where,

- U is the rotational velocity of the blade.
- W is the relative velocity.
- W_θ is the tangential component of the relative velocity.
- V is the absolute velocity.
- V_x is the axial component of the absolute velocity.

- V_θ is the tangential component of the absolute velocity.
- α is the angle between the absolute velocity and the axial axis.
- β is the angle between the relative velocity and the axial axis.

The function of the rotor is to increase the pressure of the flow by providing work, while the function of the stator is to correct the velocity triangle obtained after a rotor stage to prepare it for the next rotor stage. Since the rotational velocity of the rotor is zero, stator blades do not do work on the flow.

This interaction between flow and compressor blades in terms of energy changes can be expressed by Euler's equation. This equation is based on the conservation of energy and angular momentum. Therefore, applying this equation to the flow that crosses the blade of a compressor, torque must be the rate of change of angular momentum across the blade as it is shown in equation 21a. It can be also expressed as power in equation 21b where it has been considered, as a first approximation, that $r_2 = r_3$.

$$T = \dot{m}(V_{\theta 3} r_3 - V_{\theta 2} r_2) \tag{21a}$$

$$P = T\omega = \dot{m} U (V_{\theta 3} - V_{\theta 2}) = \dot{m} U \Delta V_\theta \tag{21b}$$

According with equation 21b, if $P \propto \Delta V_\theta = V_{\theta 3} - V_{\theta 2} > 0$, which means that tangential velocity increases across the rotor blade, work is added to the flow. It happens in compressors and this is why pressure ratio and temperature ratio increase.

4.4 Influence of swirl angle on compressor blades

Swirl appears when the flow that arrives to the rotor blades presents a nonzero swirl angle α_2. Depending on the value of this angle, velocity triangles before and after the rotor blades will change. Figure 34 shows it for both co-rotating and counter-rotating swirl.

For positive values of swirl angle (co-rotating swirl), α_2 increases and α_3 increases (but less than α_2), which means that tangential component of absolute velocity after the rotor $V_{\theta 3}$ increases less than tangential component of absolute velocity before the rotor $V_{\theta 2}$.

Taking equation 21b, $\Delta V_\theta|_{\alpha>0}$ is smaller than $\Delta V_\theta|_{clean}$, so work per unit of time is smaller than the first case without swirl. Since power given by the rotor to the flow is smaller, load over the blade decreases as well as pressure ratio and temperature ratio do from those obtained in the clean case.

However, if swirl angle is negative (counter-rotating swirl), the opposite effect appears. Swirl angle α_2 decreases and α_3 decreases too (but less than α_2), which means that tangential component of absolute velocity after the rotor $V_{\theta 3}$ decreases less than tangential component of absolute velocity before the rotor $V_{\theta 2}$.

Using again equation 21b, $\Delta V_\theta|_{\alpha<0}$ is bigger than $\Delta V_\theta|_{clean}$, so work per unit of time is bigger than first case without swirl. Since power given by the rotor to the flow increases, load over the blade also increases, as well as pressure ratio and temperature ratio do from those obtained in the clean case.

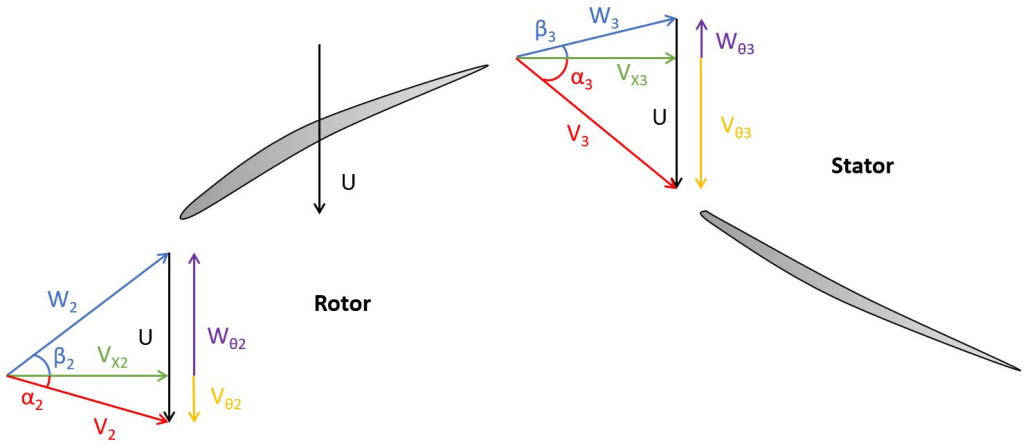

(a) Co-rotating swirl

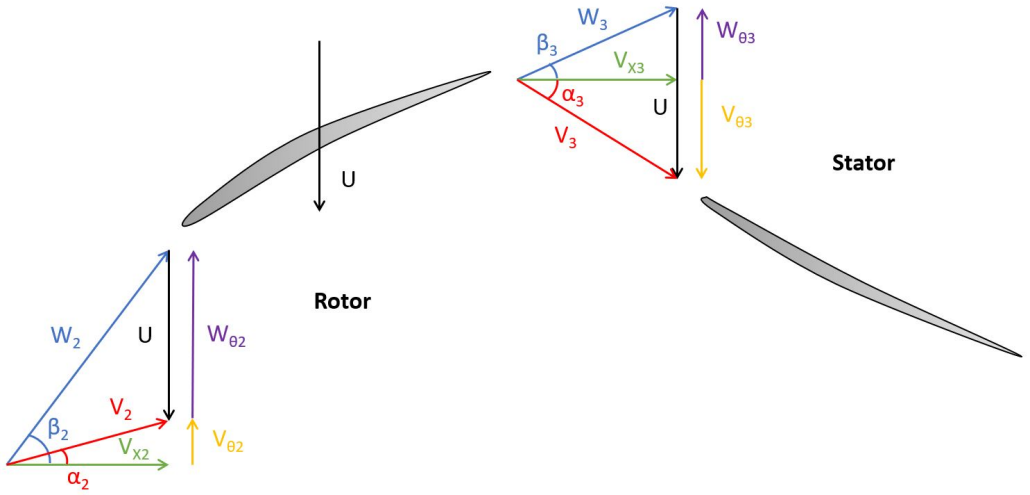

(b) Counter-rotating swirl

Figure 34: Velocity triangles before and after a rotor blade with positive and negative swirl angle.

Swirl distortion changes pressure ratio and temperature ratio, therefore it moves the speed lines of the compressor map. Figure 35 shows the impact of twin swirl, offset swirl as well as positive and negative bulk swirl on the speed lines. Compressor behavior under swirl conditions was calculated using a CFD model by Sheoran [8].

If co-rotating bulk swirl appears, pressure ratio and temperature ratio decrease, so corrected airflow decreases too. Then, the shift in speed lines is downwards in terms of pressure ratio and corrected airflow. If swirl is counter-rotating, pressure ratio and temperature ratio increase, just as the flow does. Speed lines move upwards in terms of pressure ratio and corrected airflow.

Efficiency decreases in both cases, but this change is more pronounced for counter-rotating swirl than for co-rotating swirl. This affects how much the lines on the compressor map change, so the co-rotational swirl shows a much larger decrease in pressure ratio and corrected airflow than the increments in these terms shown by the case with counter-rotational swirl.

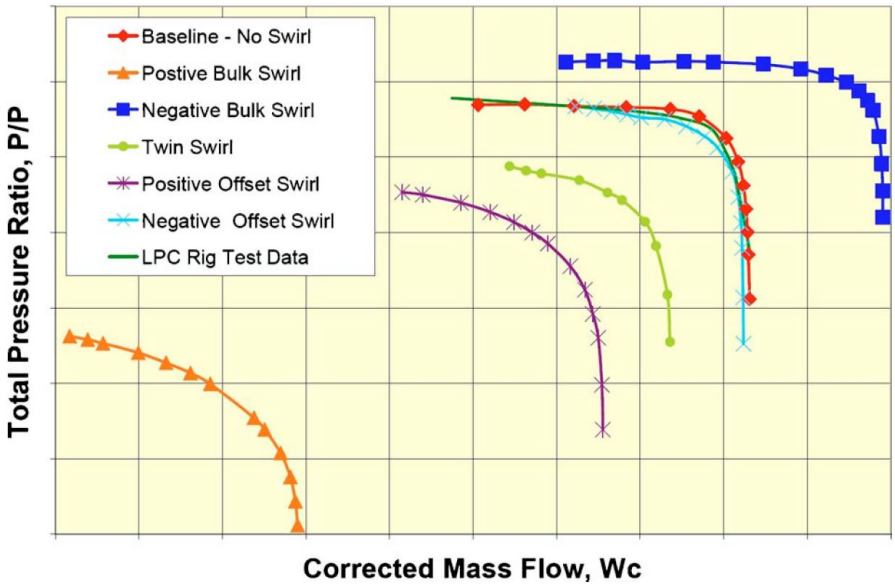

Figure 35: Speed lines for different types of swirl. Reproduced from Sheroan et al. [8]

Twin swirl consists of two equal size regions where both present different rotation directions. Thus, the speed line will be affected by the co-rotating region which decreases the pressure ratio and corrected airflow and the presence of a counter-rotating region that increases these parameters. Speed line shifts to lower pressure ratio and corrected airflow compared with the reference without swirl, but this change is smaller than what is seen for purely co-rotating bulk swirl.

Finally, the offset positive and negative swirl speed lines are also shown. In case of offset swirl, both regions are defined with opposite rotation direction but these regions have not the same size. Offset negative swirl refers to the configuration where the bigger region presents counter-rotating swirl and the smaller region co-rotating swirl. Offset positive swirl presents the opposite configuration.

Offset negative swirl speed line is similar to the clean speed line, because each region compensates for the effect of the other. Nevertheless, if offset positive swirl appears, co-rotating region has a bigger influence than counter-rotating in pressure ratio and corrected airflow so speed line shifts to lower values of both terms. The behavior of the compressor can be schematized according to the swirl angle as follows:

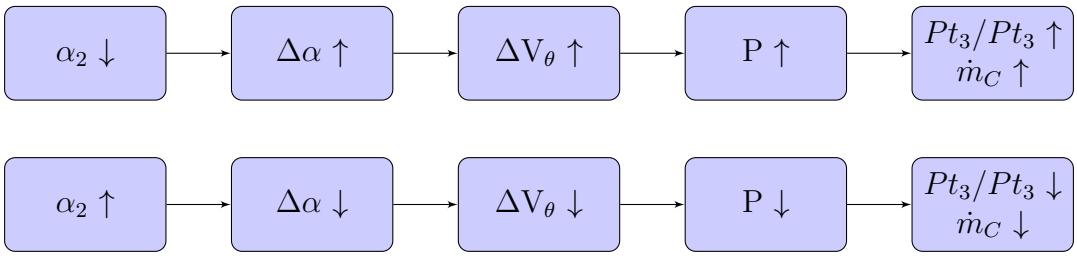

Figure 36: Shift of speed lines when swirl distortion appears.

4.5 Mean Line Code

In a first attempt to quantify this changes on speed lines, a Mean Line Code (MLC) was developed by Smith [32]. This model has been used before by some authors as Sheoran et al. [33] so it has been considered as a good option to model the behaviour of the compressor under swirl distortion.

It uses the blade geometry and inlet flow characteristics to compute outlet flow characteristics for pure bulk swirl. The model is a one-dimensional code that does not need too much information nor time to give values that represent the behaviour of the compressor.

However, the simplicity of the model means that the results that provides are not very accurate. Some assumptions have been done and justify future deviations between results obtained with MLC and other more accurate results obtained with CFD or experimental tests. Main assumptions are:

- All the flow behaves like the flow which crosses the blade at its midpoint.
- Radial influence on blade geometry is neglected.
- Efficiency changes due to swirl are neglected.
- Fluid phenomena such as boundary layer evolution or total pressure loss coefficient variation with incidence angle are neglected.

4.6 MLC implementation in MATLAB

The Mean Line Code explained before has been implemented in MATLAB to calculate the shift of speed lines when swirl distortion arrives to the compressor. This code uses compressible fluid relations to simulate modern transonic compressors.

It is based on the conservation of angular momentum across the blade to compute outlet characteristics. Deviation angle is obtained from experimental data or correlations from open literature while loss coefficient and axial velocity density ratio are computed,

P_{t2}	Total pressure	Tt_2	Total temperature
$\dot{m}$	Airflow	η_{is}	Isentropic Efficiency
N	Rotational speed	α_2	Swirl angle
β_3'	Blade metal angle	δ	Deviation angle
$r_{tip,2}$ and $r_{hub,2}$	Tip and Hub inlet radius	$r_{tip,3}$ and $r_{hub,3}$	Tip and Hub outlet radius

Table 15: Initial values needed to simulate the behaviour of the flow across the blade using MLC

The model calculates outlet pressure ratio, outlet temperature ratio and outlet absolute angle α_3, which is the angle with which the flow reaches the next stator blade. It is possible to compute also the total pressure loss coefficient ω, whose variation with the incidence angle has been neglected. The Mean Line Code needs some inputs to compute the simulation, which are shown in table 15. This process is as follows:

First, $r_{tip,2}$, $r_{hub,2}$, $r_{tip,3}$ and $r_{hub,3}$ are used to calculate the mean radius of the blade at the inlet r_2 and the outlet r_3. Area at the rotor inlet is also computed. Linear velocity U_2 and U_3 at

the mean radius are calculated using the value of rotational speed N and mean radius values r_2 and r_3.

$$r_2 = (r_{tip,2} + r_{hub,2})/2 \tag{22a}$$
$$r_3 = (r_{tip,3} + r_{hub,3})/2 \tag{22b}$$
$$A = \pi(r^2_{rip,2} - r^2_{hub,2}) \tag{22c}$$
$$U_2 = r_2 N\pi/30 \tag{22d}$$
$$U_3 = r_3 N\pi/30 \tag{22e}$$
$$\tag{22f}$$

Absolute Mach number is affected by both axial and tangential velocity components so an iterative process has to be carried out to calculate the axial component $V_{x,2}$. Equations 23 show this process in which temperature and pressure at compressor inlet have to be calculated from total conditions considering the influence of both velocity components. It allows to calculate density, which is inserted in flow equation 23a and the result of $V_{x,2}$ is compared with the supposed one until both values match. Once the iteration is finished, speed sound is also calculated. Initial $V_{x,2}$ implemented to start the iteration process is $V^0_{x,2} = \dot{m}\cdot R\cdot T_{t2}/P_{t2}\cdot A$.

$$V_{x2} = \frac{\dot{m}}{A\rho_2} \tag{23a}$$
$$V_{t2} = V_{x2}\tan\alpha_2 \tag{23b}$$
$$T_2 = T_{t2} - \frac{V^2_{x2} + V^2_{t2}}{2c_p} \tag{23c}$$
$$P_2 = P_{t2}\left(\frac{T_2}{T_{t2}}\right)^{\frac{\gamma}{\gamma-1}} \tag{23d}$$
$$\rho_2 = \frac{P_2}{RT_2} \tag{23e}$$
$$a_2 = \sqrt{\gamma RT_2} \tag{23f}$$

Then, velocity triangles are used to obtain relative conditions such as inlet absolute velocity, inlet relative velocity, inlet relative flow angle and inlet relative Mach number.

$$V_2 = V_{x2}/\cos\alpha_2 \tag{24a}$$
$$W_{t2} = U_2 - V_{x2}\tan\alpha_2 \tag{24b}$$
$$W_2 = \sqrt{V^2_{x2} + W^2_{t2}} \tag{24c}$$
$$M_{2,r} = W_2/a_2 \tag{24d}$$
$$\beta_2 = \arccos V_{x2}/W_2 \tag{24e}$$

Isentropic relationships are used again to compute inlet relative total pressure and inlet relative total temperature, which are the total conditions of the flow seen from a reference system linked to the blade.

$$P_{t2,r} = P_2\left(1 + \frac{\gamma - 1}{2} M_{2,r}^2\right)^{\frac{\gamma}{\gamma-1}} \tag{25a}$$

$$T_{t2,r} = T_2\left(1 + \frac{\gamma - 1}{2} M_{2,r}^2\right) \tag{25b}$$

Once these conditions are calculated, the relative mass flow function (MFF) at compressor inlet is needed to compute the evolution of the flow across the bladed region. $A_{\perp,W2}$ is the the area perpendicular to the relative flow.

$$MFF_{2,r} = \frac{\dot{m}\sqrt{T_{t2,r}}}{P_{t2,r} A_{\perp,W2}} = M_{2,r}\sqrt{\frac{\gamma}{R}}\left(1 + \frac{\gamma - 1}{2} M_{2,r}^2\right)^{-\frac{\gamma+1}{2(\gamma-1)}} \tag{26}$$

Besides relative mass flow function MFF; three ratios are needed to cross the bladed region: relative total temperature ratio, relative total pressure ratio, and the ratio of areas perpendicular to the flow. Deviation angle δ is obtained from experimental data or open literature, while axial density velocity ratio ADVR and total pressure loss coefficient ω are computed.

$$AVDR = \frac{r_{hub,2}^2 - r_{tip,2}^2}{r_{hub,3}^2 - r_{tip,3}^2} \tag{27a}$$

$$\beta_3 = \beta_3^{'} + \delta \tag{27b}$$

$$\frac{T_{t3,r}}{T_{t2,r}} = 1 + \frac{U_3^2 - U_2^2}{2 c_p T_{t2,r}} \tag{27c}$$

$$\frac{P_{t3,r}}{P_{t2,r}} = \left[1 + \eta_{is}\left(\frac{T_{t3,r}}{T_{t2,r}} - 1\right)\right]^{\frac{\gamma}{\gamma-1}} \tag{27d}$$

$$\left.\frac{A_2}{A_3}\right|_{\perp W} = \frac{\cos\beta_2}{\cos\beta_3} AVDR \tag{27e}$$

$$\omega = \frac{P_{t2,r} - P_{t3,r}}{P_{t2,r} - P_2} \tag{27f}$$

Thus, relative mass flow function at compressor outlet is calculated.

$$MFF_{3,r} = MFF_{2,r} \left.\frac{A_2}{A_3}\right|_{\perp W} \frac{P_{t2,r}}{P_{t3,r}} \sqrt{\frac{T_{t3,r}}{T_{t2,r}}} \tag{28}$$

Exit relative Mach number can be found iteratively.

$$MFF_{3,r} = M_{3,r}\sqrt{\frac{\gamma}{R}}\left(1 + \frac{\gamma - 1}{2} M_{3,r}^2\right)^{-\frac{\gamma+1}{2(\gamma-1)}} \tag{29}$$

Pressure, temperature, speed of sound and absolute speed after the blades can be calculated using isentropic relations.

$$P_3 = P_{t3,r}\big(1 + \frac{\gamma - 1}{2} M_{3,r}^2\big)^{-\frac{\gamma}{\gamma-1}} \tag{30a}$$

$$T_3 = T_{t3,r}\big(1 + \frac{\gamma - 1}{2} M_{3,r}^2\big)^{-1} \tag{30b}$$

$$a_3 = \sqrt{\gamma R T_3} \tag{30c}$$

$$W_3 = a_3 M_{3,r} \tag{30d}$$

Velocity components after the blade can be computed with velocity triangles so axial velocity, relative tangential velocity, absolute tangential velocity, absolute flow angle α_3 and absolute velocity after the compressor are calculated. It leads to obtain the Mach number after the compressor.

$$V_{x3} = W_3 \cos\beta_3 \tag{31a}$$

$$W_{t3} = W_3 \sin\beta_3 \tag{31b}$$

$$V_{t3} = U_3 - W_{t3} \tag{31c}$$

$$\alpha_3 = \arctan V_{t3}/V_{x3} \tag{31d}$$

$$V_3 = V_{x3}/\cos\alpha_3 \tag{31e}$$

$$M_3 = V_3/a_3 \tag{31f}$$

Total pressure and total temperature at blade outlet are calculated using isentropic relations once M_3 is known.

$$P_{t3} = P_3\big(1 + \frac{\gamma - 1}{2} M_3^2\big)^{\frac{\gamma}{\gamma-1}} \tag{32a}$$

$$T_{t3} = T_3\big(1 + \frac{\gamma - 1}{2} M_3^2\big) \tag{32b}$$

Finally, pressure ratio P_{t3}/P_{t2} and temperature ratio T_{t3}/T_{t2} are computed and form, together with the absolute flow angle α_3, the output values that characterize the flow behaviour across the blade. Since changes in corrected airflow can be computed from values of mass flow function; this code allows to estimate the shift of the compressor speed lines in function of the swirl angle.

4.7 Application case: NASA Rotor-67

4.7.1 Comparison of NASA Rotor-67 speed lines obtained with MLC and CFD

The Mean Line Code has been applied to NASA Rotor-67 and the results obtained with this one-dimensional model have been compared with those obtained with CFD simulations done by Mehdi [10]. From this reference, points of corrected speed line of 90 % and 100 % have been taken, but only the case of $N_c = 100$ % is shown in the following figures because it is the case in which simulations have been done.

Inputs requested to simulate the behaviour of the rotor are shown in table 15. In the case of NASA Rotor-67, these values have been taken from different literature sources:

- Total pressure and temperature → $P_{t2} = 101.325$ Pa and $T_{t2} = 288.15$ K
- Isentropic efficiency → $\eta_{is} = 90$ % [10]
- Rotational speed (for $N_c = 100$ %) → N = 16043 rpm [19]
- Mach number → $M_2 = 0.8$
- Blade metal angle → $\beta_3' = 12°$
- Deviation angle → $\delta = 8°$
- Blade geometry → $r_{tip,2} = 51.4$ cm, $r_{hub,2} = 9.6$ cm, $r_{tip,3} = 48.5$ cm, $r_{hub,3} = 9.7$ cm [10]

Blade metal angle chosen was $\beta_3' = 12°$, which is approximately the mean value between hub and tip regarding Koning [34]. Deviation angle chosen was $\delta = 8°$, because it is a typical value of this magnitude following the results obtained by Miller [35]. Regarding to isentropic efficiency, a value of $\eta_{is} = 90$ % has been chosen because is the value obtained by Mehdi [10] for clean conditions.

Swirl angle α_2 takes different values because the aim of the simulation is to see the influence of different swirl angles on compressor behaviour. Simulation has been done for $\alpha_2 = 5°$, $10°$, $15°$ and $20°$. The airflow chosen is the interval between the one corresponding to the point of highest pressure ratio, $\dot{m}_{corr} = 32.4$ kg/s; and the one corresponding to the point of lowest pressure ratio $\dot{m}_{corr} = 34.6$ kg/s.

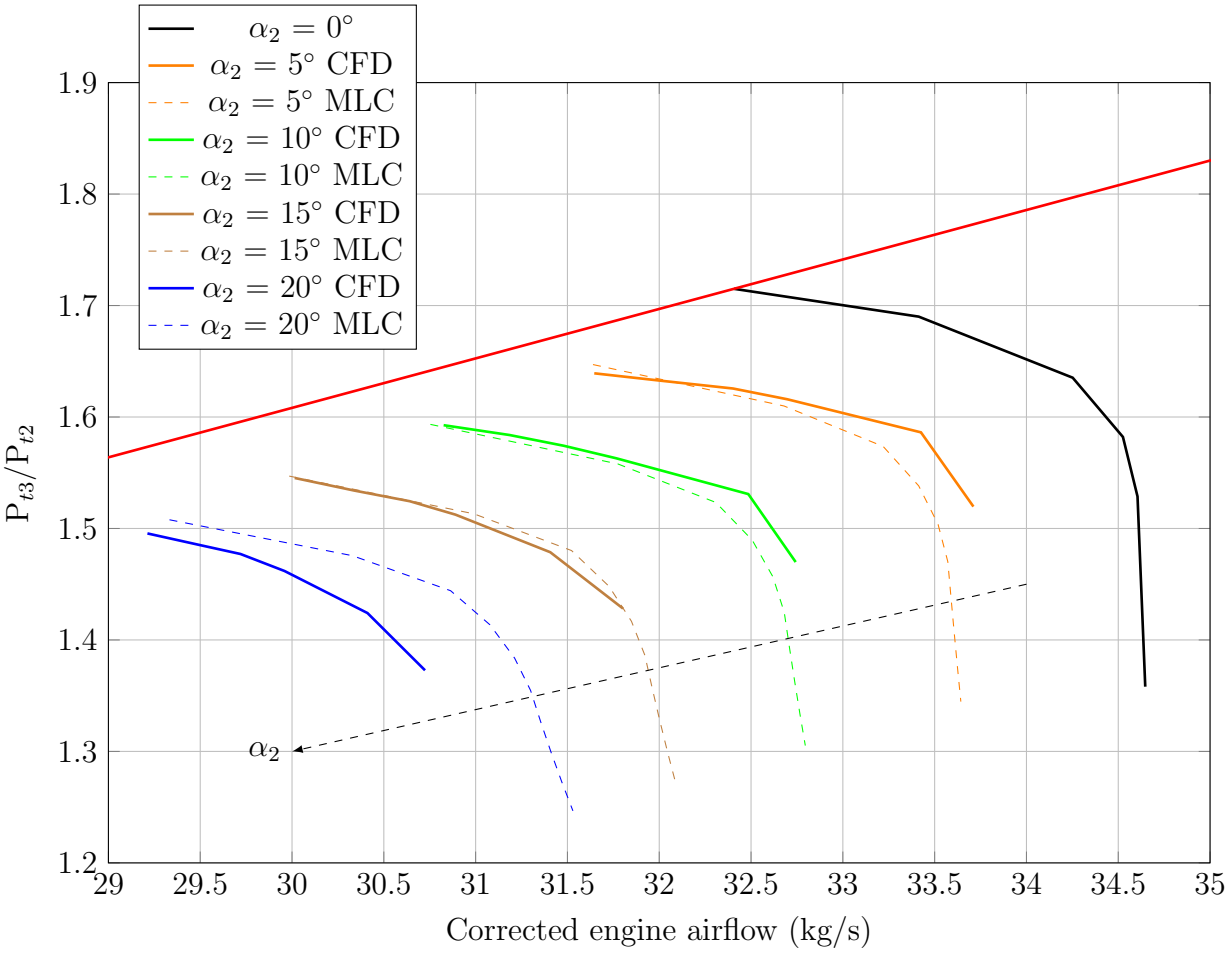

Figure 37: Speed lines of Rotor-67 with swirl distortion calculated with MLC and CFD simulations.

Figure 37 shows the rotor map with clean inlet conditions and results obtained using the Mean Line Code (dashed lines) and those obtained with CFD simulations developed by Mehdi [10]. Theoretically, CFD results are more accurate than those obtained with MLC because they take into account radial effects, efficiency changes or some fluid phenomena that were neglected in the Mean Line Code.

Results obtained with MLC are similar to values calculated with CFD so they can be used as a first approximation to understand the influence of swirl distortion on the compressor and to estimate a fast solution. This is a good result considering the hypothesis done and also that only a few geometric parameters of the blade were necessary to perform the simulation.

4.7.2 Results of NASA Rotor-67

Once the Mean Line Code has proved that speed lines computed with swirl distortion follow the expected trend, some calculations have been carried out to understand the influence of swirl distortion in compressor performance and stability.

Firstly, maximum and minimum pressure ratio and corrected engine airflow of calculated speed lines have been computed. Figure 38 shows that when swirl angle increases, maximum and minimum values of pressure ratio decrease. Corrected airflow follows the same trend, decreasing when α_2 increases.

This behavior is expected in the presence of swirl distortion where swirl angle is positive because, regarding equation 21, when swirl angle increases, work done on the fluid decreases so pressure ratio and corrected airflow also do.

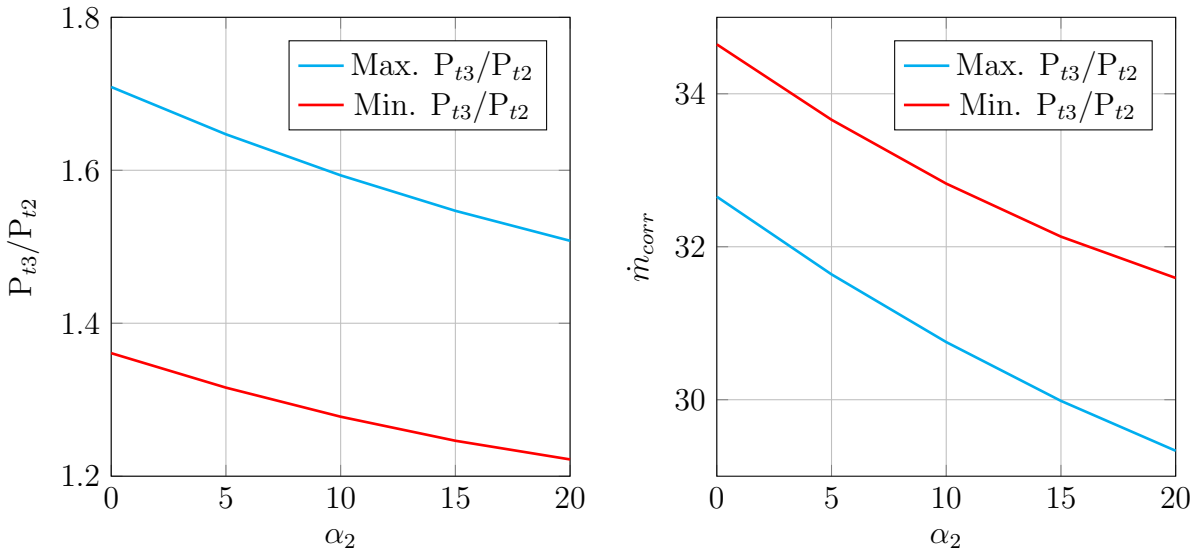

(a) Pressure ratio

(b) Corrected airflow

Figure 38: Maximum and minimum values of pressure ratio and corrected airflow for different α_2.

The Mean Line Code calculates also the total pressure loss coefficient ω, which has been defined previously in equation 27f. Results obtained are shown in Figure 39. It increases when swirl distortion increases, going from $\omega = 6$ % when there is not swirl distortion to $\omega = 8$ % for values of $\alpha_2 = 20°$.

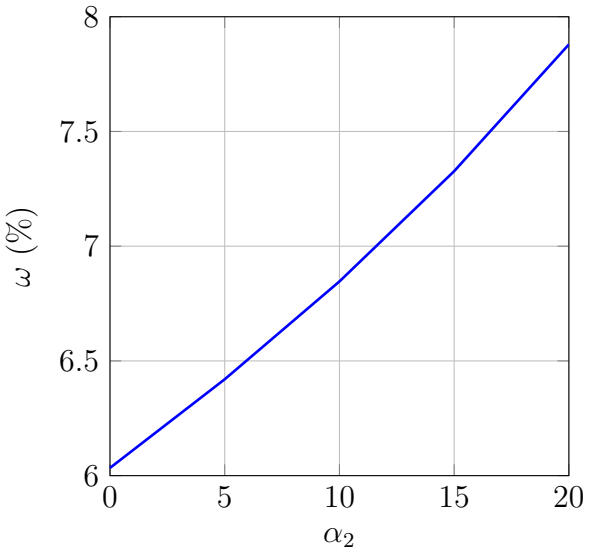

Figure 39: Total pressure loss coefficient for different α_2.

To study the influence of swirl distortion on compressor stability, surge margin of clean and distorted cases have been calculated. The study has been carried out studying the surge margin for constant corrected airflow, which has been defined as follows:

$$SM = \frac{PR_{SL} - PR_{Nc}}{PR_{Nc}} \ 100 \ \% \tag{33}$$

Where PR_{Nc} is the pressure ratio of the studied point in the chosen speed line and PR_{SL} is the pressure ratio of the surge line point which has the same value of corrected airflow than the studied one.

Both analytical and numerical (those obtained from reference [10]) speed lines represented in figure 37 have been computed to obtain the surge margin of these lines, which is shown in figure 40. No important differences have been found between numerical and analytical results for swirl angles of $\alpha_2 = 15°$, $\alpha_2 = 10°$and $\alpha_2 = 15°$. Conversely, considerable differences have been found in the simulations carried out with $\alpha_2 = 20°$.

When there is not swirl distortion (black line), surge margin is 0 % for the point of higher pressure ratio and surge margin increases up to more than 30 % when pressure ratio decreases when moving along the speed line. This trend is also maintained when there is swirl distortion.

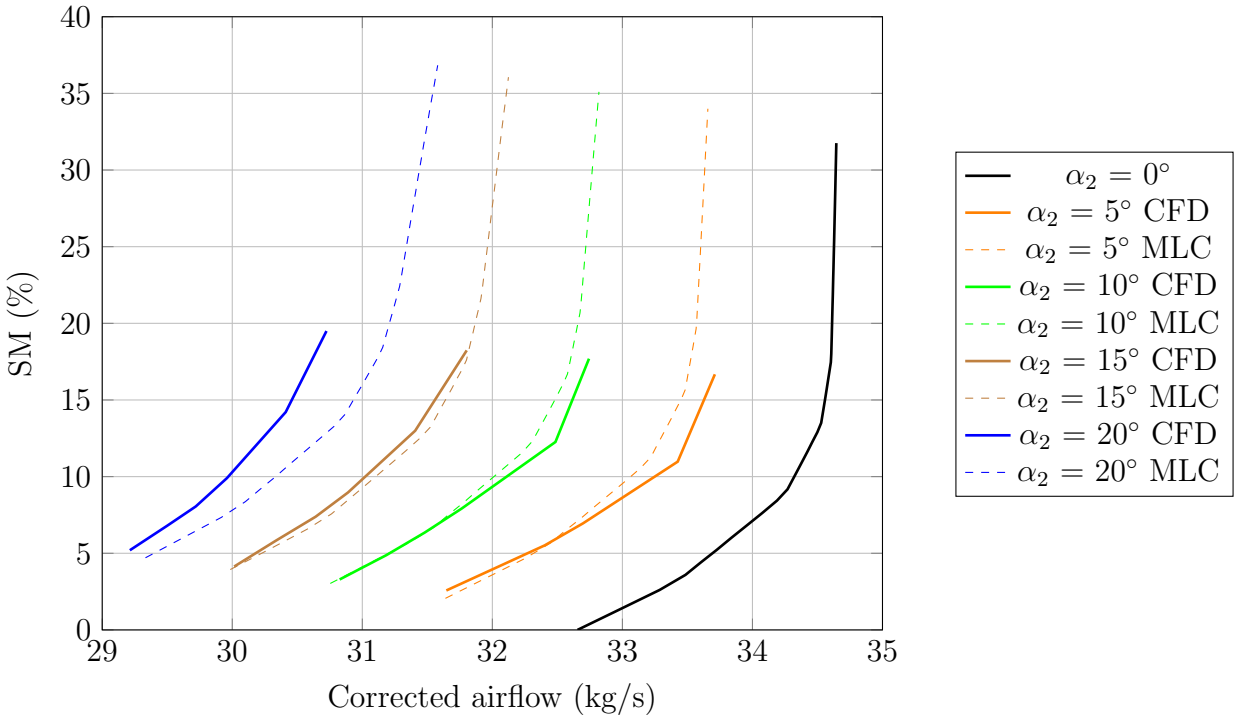

Figure 40: Surge margin evolution with corrected airflow for different α_2.

If swirl distortion arrives to the compressor inlet, the speed lines move towards lower pressure ratio and corrected airflow values. This change moves the new lines away from the surge line, so the surge margin increases. For example, when $\alpha_2 = 10°$, surge margin is 3 % for the highest pressure ratio and 35 % for the lowest pressure ratio.

In order to quantify the variation of the surge margin with swirl distortion, surge margin of the highest pressure point of each corrected speed has been computed both for analytical (MLC) and numerical (CFD) results, which is shown in figure 41. As it has been explained, surge margin increases when swirl distortion increases. Analytical and numerical results are similar, giving a slightly higher value of surge margin in the numerical case.

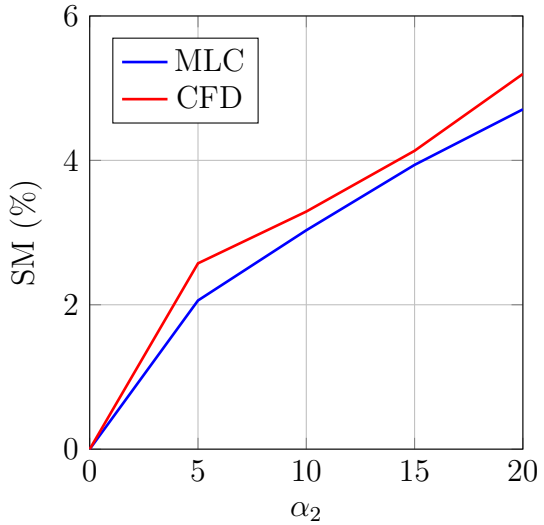

Figure 41: Surge margin of the highest pressure point for different α_2.

5 Temperature Distortion - Effect on compressor stability

Temperature distortion has been studied more in detail for military applications, where it is more common for the engine to ingest hot gases that result in a distortion in temperatures. Gun and missile gas ingestion should be considered, in the same way that helicopters or vertical take-off planes. In civil aviation, temperature distortion may occur due to ingestion of hot gases from other aircraft or reversal thrust during landing.

5.1 Circular temperature distortion

Total temperature distortion descriptor is similar to pressure distortion descriptor presented above, but considering that in this case, the critical region is the high temperature region. Figure 42 represents it. Equations to calculate both intensity and extent of the high temperature region are:

$$\theta_i^+ = \theta_{2i} - \theta_{1i} \tag{34a}$$

$$\left(\frac{\Delta TC}{T}\right)_i = \left(\frac{T_{AVHIGH} - T_{AV}}{T_{AV}}\right)_i \tag{34b}$$

$$T_{AVi} = \frac{1}{360}\int_0^{360} T(\theta)_i \, d\theta \tag{34c}$$

$$T_{AVHIGHi} = \frac{1}{\theta_i^-}\int_{\theta_{1i}}^{\theta_{2i}} T(\theta)_i \, d\theta \tag{34d}$$

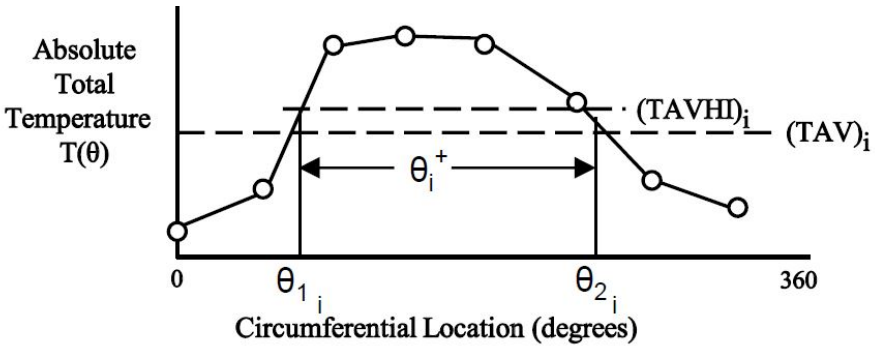

Figure 42: Ring Circumferential Distortion for a One-Per-Revolution Pattern. Reproduced from Cousins et al. [12].

5.2 Radial temperature distortion

The radial temperature distortion has the same structure that pressure distortion defined before, and it is done by calculating the difference between the average pressure of the ring and the average pressure of the AIP. It is possible to have both positive and negative values, where positive values refer to the rings whose pressure is lower than the average.

$$\left(\frac{\Delta TR}{T}\right)_i = \frac{T_{AIP} - T_{AVi}}{T_{AIP}} \tag{35}$$

Because most of the investigations carried out regarding the temperature distortion indices are military, no other indices have been found to measure this phenomenon.

5.3 Parallel compressor model for temperature

Parallel compressor model can be also applied to temperature distortion as Kurzke [13] proposes. Even so, this model has not been widely used by authors to estimate compressor behavior because temperature distortion has not been studied as deeply as pressure and swirl distortion.

As it has been explained before, the critical region when temperature distortion appears is the high temperature region. Figure 43 shows a typical temperature distortion pattern and the operating points of both regions.

In figure 43 an example of a compressor map is also represented to analyse qualitatively the response of the compressor against temperature distortion. Operation points move for different clean or distorted conditions keeping constant pressure ratio. Clean operation point (M) is represented in its corrected speed line. The compressor with lower temperature (L) operates with in a higher corrected speed line, while the compressor with higher temperature (H) operates with in a lower corrected speed line.

When distortion increases, both operation points move away from each other to keep the same static pressure at the compressor outlet, until the high temperature operation point reaches the clean surge line, moment in which the instability is considered to appear.

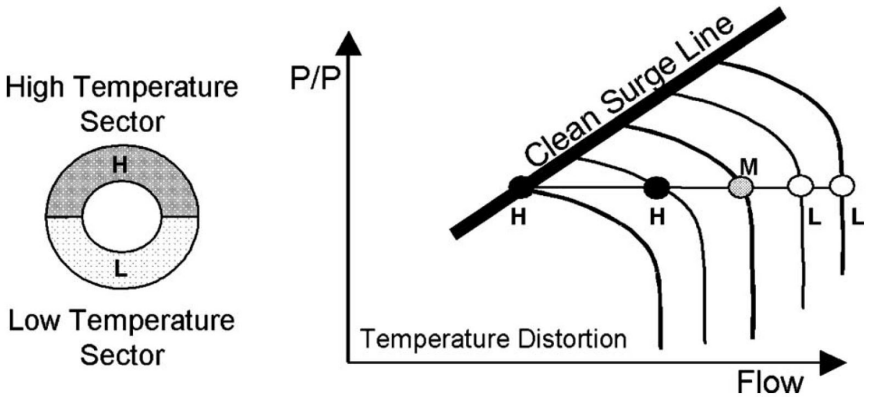

Figure 43: Temperature distortion pattern and operating points. Reproduced from Kurzke et al. [13].

5.4 PCM for temperature implementation in MATLAB

In order to estimate the changes in surge margin with temperature distortion, parallel compressor model for temperature has been implemented in MATLAB. This model has been applied to the compressor of the PW-1128 and results obtained have been compared with other results obtained experimentally. Finally, some estimations of the compressor behaviour under other distortion conditions are presented.

Figure 44 shows the compressor map of the engine. The red line is the surge line, the black line is the steady state line and the blue lines represent the corrected speed lines for values between 80 % and 102 % of design.

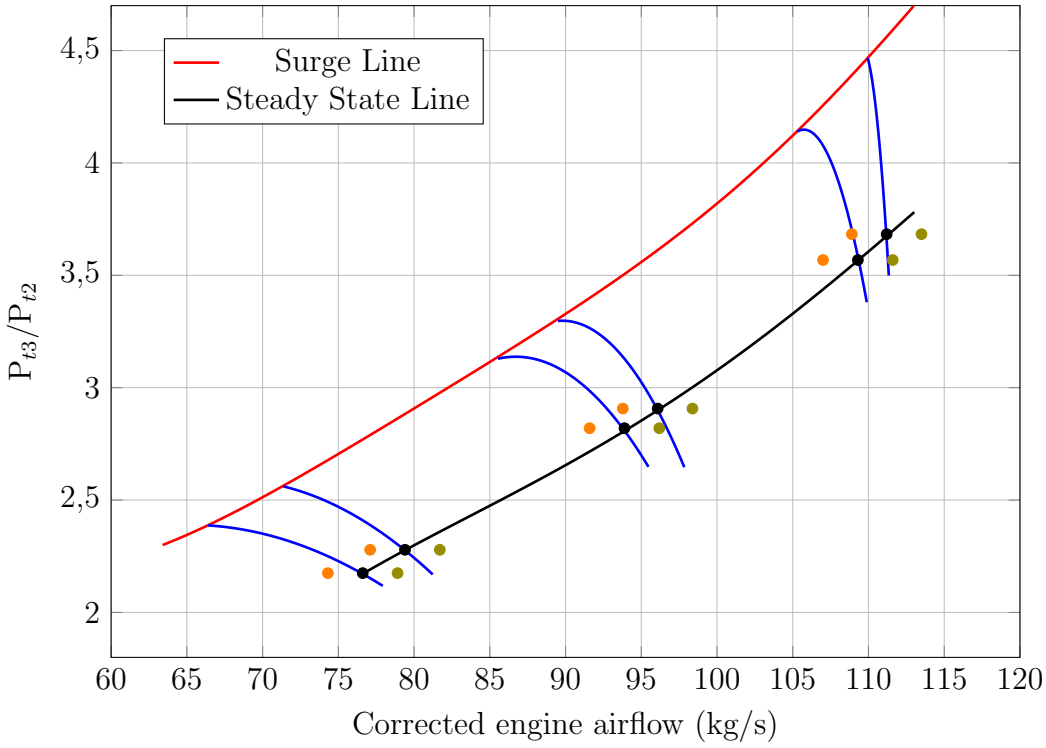

Figure 44: LPC map of PW-1128 engine.

When a distorted flow enters through the compressor, the parallel compressor model is applied to the points of the steady state line. This distortion leads two operation points, one for each region with different values of static pressure at the compressor discharge ($P_{3,S}$). This value is studied for several pairs of points, increasingly separated from each other; until a pair whose $P_{3,S}$ values match is found. The orange point refers to the high temperature region while the green one refers to the low temperature region.

$\dot{m}$	Airflow	P_{t3}/P_{t2}	Pressure ratio
P_0 and T_0	Ambient conditions	M	Mach number
ΔT_{t2}	Temperature distortion	A	Compressor area
RR	Ram Recovery	η_{is}	Isentropic efficiency

Table 16: Initial values needed to calculate the operating point with distortion

The process for calculating the static pressure at the compressor discharge needs some values related with compressor operation conditions, ambient conditions, characteristics of the distortion and characteristics of the engine. These values are shown in table 16. This process is as follows:

From ambient conditions P_0 and T_0, Mach number M and ram recovery RR, it is possible to

calculate total pressure and total temperature conditions at AIP:

$$P_{t0} = P_0\left(1 + \frac{\gamma - 1}{2}M^2\right)^{\frac{\gamma-1}{\gamma}} \tag{36a}$$

$$P_{t2} = P_{t0}RR \tag{36b}$$

$$T_{t2} = T_{t0} = T_0\left(1 + \frac{\gamma - 1}{2}M^2\right) \tag{36c}$$

High temperature can be computed from ΔT_{t2}, which is the difference between high and low temperature sectors (where $T_{t2} = T_{t2,Low}$).

$$T_{t2,High} = T_{t2} + \Delta T \tag{37}$$

Distortion can be also characterized by circular temperature distortion. Therefore, with high and low temperatures, $\Delta TC/T$ is computed.

$$T_{AVHIGH} = T_{t2,High} \tag{38a}$$

$$T_{AV} = \frac{T_{t2,High} + T_{t2,Low}}{2} \tag{38b}$$

$$\frac{\Delta TC}{T} = \frac{T_{AVHIGH} - T_{AV}}{T_{AV}} \tag{38c}$$

Operation point is characterized by its pressure ratio P_{t3}/P_{t2} and corrected airflow $\dot{m}_{corr}$. Using the first one, together with isentropic efficiency of the compressor, total conditions at compressor discharge are computed. It is important to indicate that there will be two values of T_{T3}, one for each value of T_{T2}.

$$P_{t3} = \pi_{2,3}P_{t2} \tag{39a}$$

$$\frac{T_{t3}}{T_{t2}} = 1 + \frac{\pi_{2,3}^{\frac{\gamma-1}{\gamma}} - 1}{\eta_{is}} \tag{39b}$$

Once T_{t3} and P_{t3} are calculated, static pressure at compressor discharge is determined from Mach number which was obtained using the relation:

$$\frac{\dot{m}\sqrt{\gamma RT_{t3}}}{\gamma P_{t3}A} = \frac{M}{\left[1 + \left(\frac{\gamma-1}{2}\right)M^2\right]^{(\gamma+1)/2(\gamma-1)}} = \frac{M}{(1 + 0.2M^2)^3} \tag{40}$$

With the Mach at compressor discharge and Pt3, static pressure is calculated:

$$P_{3,S} = \frac{P_{t3}}{\left(1 + \frac{\gamma-1}{2}M^2\right)^{\frac{\gamma-1}{\gamma}}} \tag{41}$$

This process is done with both high and low temperature points and its values of static are compared. While these values are different, both points move away each other until a pair of points have the same static pressure $P_{3,S}$ at compressor discharge.

When a distorted flow enters through the compressor, the surge line moves closer to the steady state line. It is possible to calculate the modified surge line as a function of the distortion by searching the first point of the corrected speed line for which its high temperature point is above the surge line.

With both points, the original point which produces the situation imposed with the defined distortion is the point for which surge will appear. Surge margin is defined by taking in count the difference in pressure ratio between the steady state line (SSL) and the surge line (SL) which is in the vertical of the first:

$$SM(\%) = \frac{PR_{SL} - PR_{SSL}}{PR_{SSL}} \ 100 \ \% \tag{42}$$

5.5 Application case: PW-1128 Low Pressure Compressor

5.5.1 Validation of PW-1128 LPC

The parallel compressor model for temperature presented above has been validated by comparing the calculated results with those obtained experimentally by Mehalic [28].The model has been applied to find the surge line analytically with the same conditions than those used during tests:

- Altitude $\rightarrow$ h = 30.000 ft = 9144 m $\rightarrow$ P_0 = 30.088 Pa and T_0 = 228.7 K
- Mach $\rightarrow$ M = 0.8 $\rightarrow$ P_{T0} = 45.854 Pa and T_{T0} = 258 K
- Ram Recovery $\rightarrow$ RR = 0.99 $\rightarrow$ P_{T2} = 45.406 Pa
- Isentropic efficiency $\rightarrow$ $\eta_{is} = 0.8$

Ram recovery chosen was 0.99, a typical value for inlets nowadays. About isentropic efficiency of the compressor, η_{is} = 80 % has been chosen as a typical value of low pressure compressors in the absence of information regarding this compressor property. In this case, both sector have the same angle of 180°.

In the reference from which experimental results were presented, they are presented as a compressor map with the experimental surge line obtained for different values of circular distortion indexes depending on the corrected speed line. Figure 45 shows the results obtained experimentally and also the surge line calculated with the implemented model.

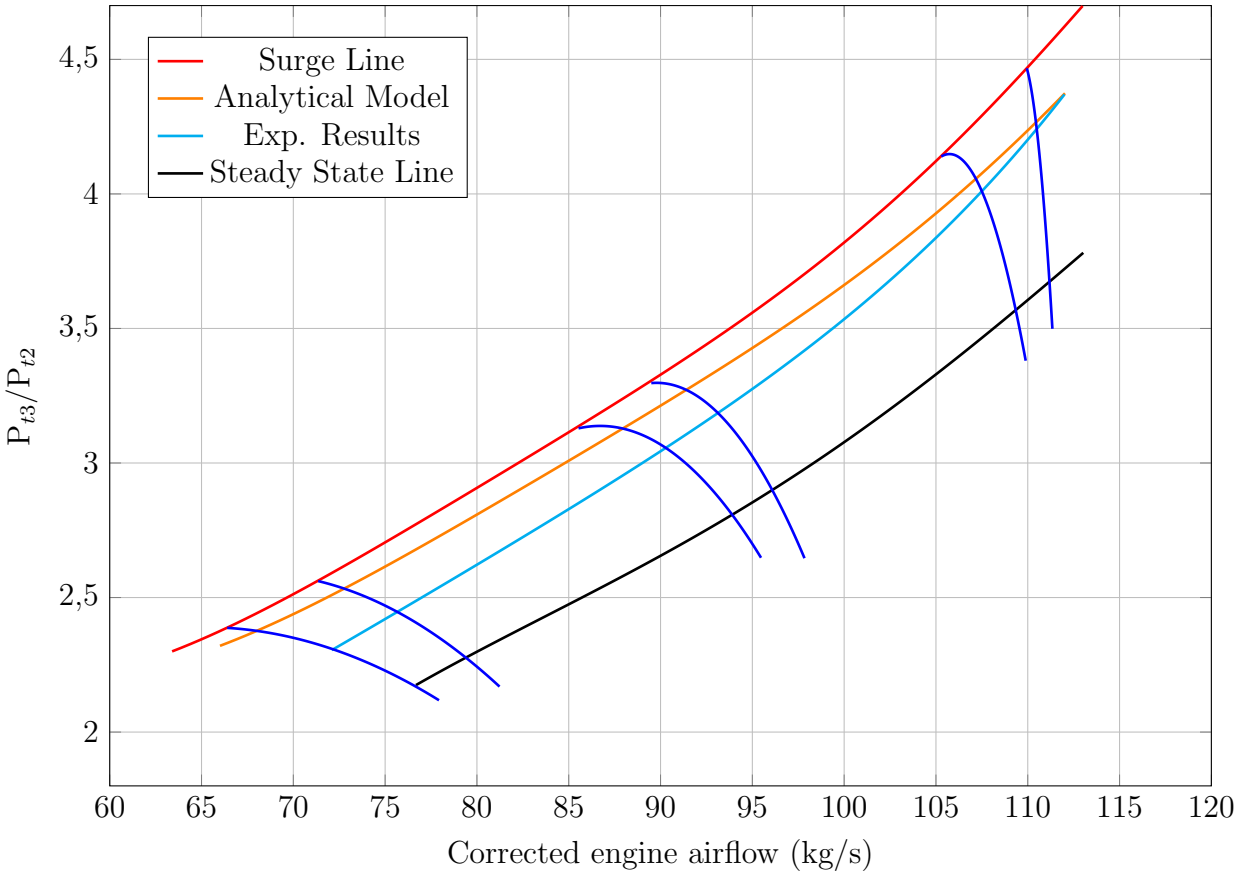

Figure 45: LPC map of PW-1128 engine with the experimental surge line and the calculated one with the model proposed for temperature distortion.

Results calculated analytically are close to those obtained experimentally only for corrected speed values around 100 % of design value. Table 17 shows the differences in percent loss of surge pressure ratio ΔPRS for both analytical and experimental results.

	Nc = 80 %		Nc = 90.1 %		Nc = 100.2 %	
	PR	ΔPRS	PR	ΔPRS	PR	ΔPRS
Clean SL	2.78	-	3.50	-	4.42	-
An. SL	2.68	3.6 %	3.38	3.4 %	4.19	5.2 %
Exp. SL	2.49	10.4 %	3.23	7.7 %	4.15	6.1 %
Error	6.8 %		4.3 %		0.9 %	

Table 17: Pressure ratio and percent loss of surge pressure ratio variation from clean surge line to distorted surge line for temperature distortion.

The first conclusion obtained from the compressor map is confirmed with this table, where the error between experimental and analytical results decreases when corrected speed increases. While for N_C = 80 %, the error is 6.8 % and for N_C = 90.1 %, the error is 4.3 %; when N_C = 100.2 %, the error is 0.9 %. This last case is the only one whose error allows to state that the results obtained analytically accurately represent the behavior of the compressor under temperature distortion.

5.6 Results of PW-1128 LPC

After comparing analytical and experimental results, this model can be used to estimate the behaviour of the compressor with temperature distortion around design corrected speeds.

Due to the infuence of distortion, the surge line approaches the steady state line when distortion increases. Some values between $CDI_{mean} = 0$ (clean section) and $CDI_{mean} = 10$ % have been chosen to calculate the variation of the surge line with CDI. Figure 46 shows the clean surge line in red, for which CDI = 0 and other lines that represent different values of CDI. This figure is represented only for values of corrected airflow related with corrected speeds above 95 % of design value, for which the model provides good results.

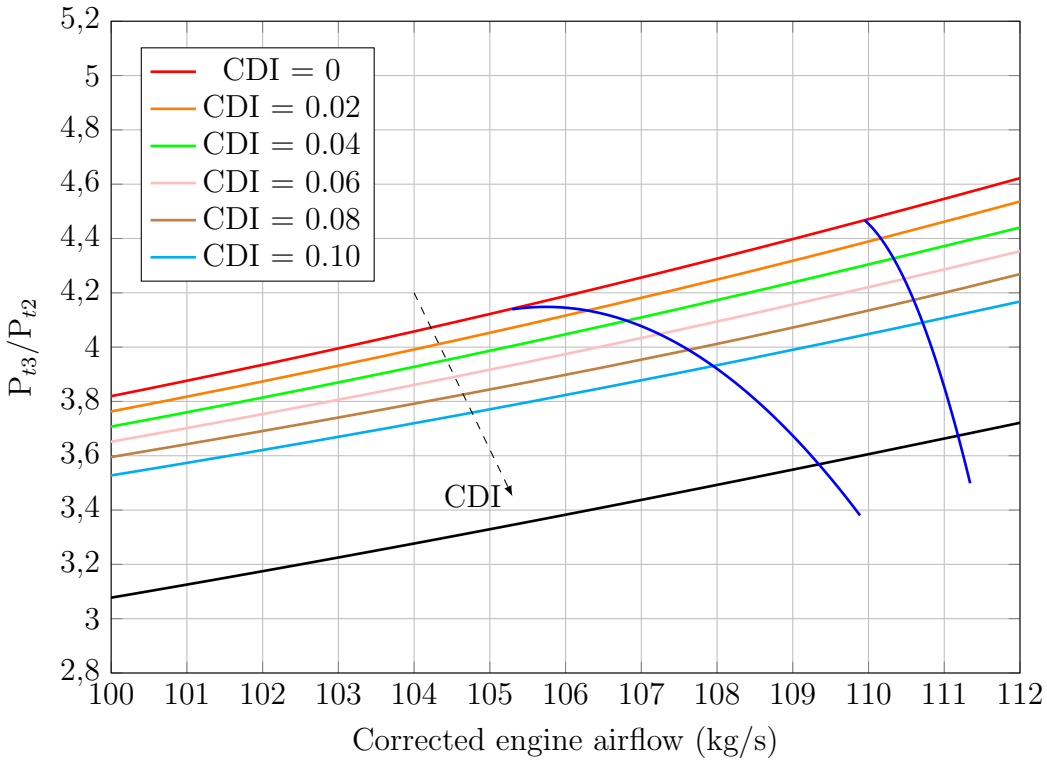

Figure 46: LPC map of PW-1128 engine with the calculated surge line for different temperature distortion conditions.

This figure is summarized in table 18, where percent loss of surge pressure ratio ΔPRS is calculated for different distortion values for a given operation point of the steady state line corresponding to a corrected speed of $N_C = 100$ %.

CDI	0	0.02	0.04	0.06	0.08	0.10
ΔPRS	0 %	1.8 %	3.8 %	5.7 %	7.5 %	9.3 %

Table 18: Percent loss of surge pressure ratio for different temperature distortion conditions.

Loss of surge pressure ratio increases when distortion increases, which fits with the expected because, the bigger the distortion, the lower the pressure ratio for which surge appears.

Surge margin evolution is also presented in figure 47. As expected, when distortion increases, surge margin decreases. The reason is that the operation point of the high temperature region approaches the surge line so the point in which surge appears has smaller pressure ratio. Therefore, the distorted surge line is below the clean one and closer to the steady state line.

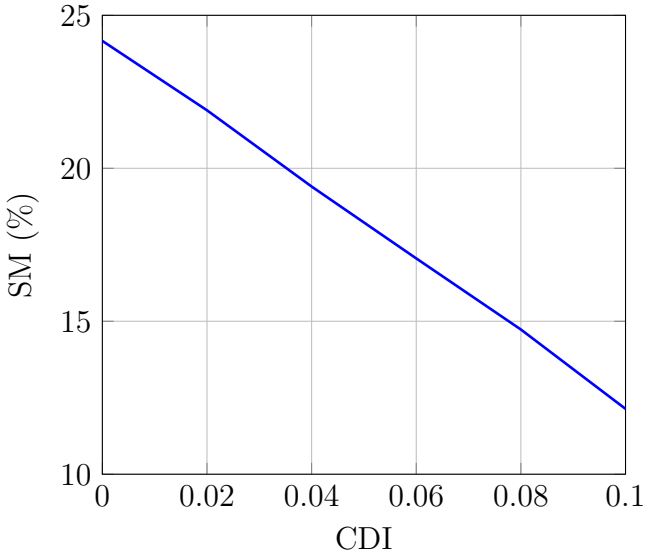

Figure 47: Surge margin evolution with CDI for N_C = 100.2 %.

Values from this figure correspond to the same point than those of table 18. In this case, when there is no temperature distortion, surge margin is around 24 %. However, values of CDI = 0.10 cut in a half the surge margin, giving values of SM = 12 %.

This tool is able to estimate the behaviour of the compressor under temperature distortion for some values of corrected speed. Even it could be enough to understand the main effects of this type of distortion on compressor stability, this tool is not accurate enough to reproduce with reliability the compressor response under these conditions.

6 Conclusions

Stability of engines against stall and surge is related with pressure, swirl and temperature distortion at the Aerodynamic Interface Plane. Distortion indexes are essential tools for quantifying the distortion.

There are different types of distortion indexes, proposed by engineering societies and companies. Four examples from reference [4] have been used to study how each pressure index adapts to different distortion patterns. Different results have been obtained for all of them. Even KD_2 and KA_2 mix circumferential and radial distortion, there is hardly any information about how both can be related with compressor stability. Considering Rolls-Royce's studies where it has been proved that circumferential distortion is much more detrimental than radial in relation with surge, and some information of experimental tests given in reference [7], CDI_{mean} has been chosen as the index used to relate the surge margin to pressure distortion.

The parallel compressor model has been used to study the behaviour of an engine when a distortion enters through the compressor. An analytical model has been implemented in MATLAB and it has been verified that the calculated results agree with those obtained experimentally for Larzac04 [7] and PW-1128 [28]. As expected, surge margin decreases when corrected speed increases, and also when circumferential distortion index does. Therefore, it will be important to evaluate the distortion present in all the flows entering the engine during its operation to avoid surge.

The effects of swirl distortion on compressor performance and stability have been also studied. Firstly, this type of distortion has been defined and characterized. Then, the Mean Line Code has been implemented in MATLAB to simulate the behaviour of the compressor under pure bulk swirl conditions for both co-rotating and counter-rotating cases. Results obtained agree with those obtained with CFD by Mehdi [10], which have been used as a comparison-based reference. When swirl distortion appears, corrected speed lines move on the compressor map, so for co-rotating swirl they move downwards and leftwards, decreasing pressure ratio and increasing surge margin. However, for counter-rotating swirl, speed lines move upwards and rightwards, increasing pressure ratio and decreasing surge margin.

Finally, the effect of temperature distortion have been studied. Significant indexes have been defined to characterize this type of distortion and a modified version of parallel compressor model for temperature has been implemented in MATLAB. Results calculated have been compared with those obtained experimentally for PW-1128 [28]. These results calculated with the model agree with experimental results only for high values of the corrected speed so the model has only been used to estimate surge margin for these corrected speeds. When temperature distortion increases, surge line move downwards approaching steady state line so surge margin decreases.

Returning to the objectives presented at the beginning of this thesis, all of them have been fulfilled: A review of pressure distortion indexes has been performed, together with its effect on compressor stability. Swirl distortion has been defined and characterized, evaluating its influence on compressor performance and stability. Temperature distortion has been also defined and its impact on compressor stability has been estimated. All this has been done through codes in MATLAB which are attached to this thesis, providing a kit of tools to estimate compressor behaviour under distortion.

References

[1] M.P. Boyce. *Combined Cycle Systems for Near-Zero Emission Power Generation*, chapter 2, pages 44–102. Woodhead, 2012.

[2] Mark L. Celestina and Mary J. Long-Davis. Large-scale Boundary Layer Ingesting Propulsor Research. *ISABE Conference*, 9 2019. ISABE-2019-24264.

[3] Society of Automotive Engineers. Gas Turbine Engine Inlet Flow Distortion Guidelines. 2002.

[4] J. Pecinka, G. T. Bugajski, P. Kmoch, and A. Jilek. Jet Engine Inlet Distortion Screen and Descriptor Evaluation. *Acta Polytechnica*, 57(1):22–31, 2017. DOI:10.14311/AP.2017.57.0022.

[5] Joachim Kurzke and Ian Halliwell. *Propulsion and Power*, chapter 6, pages 249–267. Springer, 2018.

[6] Manish Pokhrel, Jonathan Gladin, Elena Garcia, and Dimitri N. Mavris. A methodology for quantifying distortion impacts using a modified parallel compressor theory. 2018. GT2018-77089.

[7] Rudolf. P. M. Rademakers, Stefan Bindl, and Reinhard Niehuis. Effects of Flow Distortions as They Occur in S-Duct Inlets on the Performance and Stability of a Jet Engine. *Journal of Engineering for Gas Turbines and Power*, 138, 2 2016. An optional note.

[8] Yogi Sheoran, Bruce Bouldin, and P. Murali Krishnan. Compressor Performance and Operability in Swirl Distortion. *Journal of Turbomachinery*, 134, 7 2012. DOI:10.1115/1.4003657.

[9] J.P. Murphy and D.G. MacManus. Inlet ground vortex aerodynamics under headwind conditions. *Aerospace Science and Technology*, pages 207–215, 2011. DOI:10.1016/j.ast.2010.12.005.

[10] Ahad Mehdi. *Effect of Swirl Distortion on Gas Turbine Operability*. PhD thesis, School of engineering - Power and Propulsion Department. Crandfield University, 5 2014.

[11] Society of Automotive Engineers. A methodology for assessing inlet swirl distortion. 2007. Technical Report AIR5686.

[12] William T. Cousins and Milt W. Davis. Evaluating complex inlet distortion with a parallel compressor model: Part 1 - Concepts, theory, extensions and limitations. *ASME Turbo Expo*, 2011. GT2011-45067.

[13] Joachim Kurzke. Effects of Inlet Flow Distortion on the Performance of Aircraft Gas Turbines. *Journal of Engineering for Gas Turbines and Power*, 130, 7 2008. DOI:10.1115/1.2901190.

[14] H. Pearson and A.B. McKenzie. Wakes in Axial Compressors. *The Journal of the Royal Aeronautical Society*, 63:415–416, 1959. DOI:10.1017/S0368393100071273.

[15] C. Reid. The Response of Axial Flow Compressors to Intake Flow Distortion. *ASME*, 1969.

[16] Annette Flanagan Campbell. An investigation of distortion indices for prediction of stalling behavior in aircraft gas turbine engines. Master's thesis.

[17] Jakob P. Haug and Reinhard Niehuis. Full Annulus Simulations of a Transonic Axial Compressor Stage with Distorted Inflow at Transonic and Subsonic Blade Tip Speed. *International Journal of Turbomachinery Propulsion Power*, 2 2018. DOI:10.3390/ijtpp3010007.

[18] Kaili Liu, Yifeng Sun, Yuan Zhong, Huiliu Zhang, Kunyuan Zhang, and Hui Yang. Numerical investigation on engine inlet distortion under crosswind for a commercial transport aircraft. *Congress of the International Council of Aeronautical Sciences*, 9 2014.

[19] A. Naseri, M. Boroomand, and S. Sammak. Numerical Investigation of Effect of Inlet Swirl and Total-pressure Distortion on Performance and Stability of an Axial Transonic Compressor. *Journal of Thermal Science*, 25(6):501–510, 7 2016. DOI:10.1007/s11630-016-0891-6.

[20] B.J.Lee, May-Fun Liou, and M. Celestina. Conceptual Design of a Counter-Rotating Fan System for Distributed Boundary Layer Ingesting Propulsion. *ISABE Conference*, 9 2019. ISABE-2019-24285.

[21] Ryo Kagaya, Yoshinori Ooba, and Shinya Kusuda. Numerical Prediction of Fan Performance Response with Inlet Distortion of Aircraft Engines. *ISABE Conference*, 9 2019. ISABE-2019-24086.

[22] O. Sharma J. Berton L. Hardin, G. Tillman and D. Arend. Aircraft System Study of Boundary Layer Ingesting Propulsion. *American Institute of Aeronautics and Astronautics*, 2012. AIAA-2012-3993.

[23] Patrick Hendrick. *Aircraft propulsion*, chapter 2.

[24] D.L. Hughes, L.P. Myers, and K.G. Mackall. Effects of Inlet Distortion on a Static Pressure Probe Mounted on the Engine Hub in an F-15 Airplane. Technical report, National Aeronautics and Space Administration - NASA, Ames Research Center, 4 1985. NASA TP-2411.

[25] C.H. Stevens, E.D. Spong, and MS. Hammock. F-15 Inlet/Engine Test Techniques and Distortion Methodologies Studies. Technical report, NASA - National Aeronautics and Space Administration, 1978.

[26] Edward J. Milner. Analytical prediction of the performance and stability of a J85-13 compressor with distorted inlet flow. Technical report, National Aeronautics and Space Administration - NASA, Lewis Research Center, 5 1977. NASA TM X-3515.

[27] J.P. Longley and E.M. Greitzer. Inlet distortion effects in aircraft propulsion system integration. Technical report, National Aeronautics and Space Administration - NASA, 5 1992.

[28] Charles M. Mehalic. Effect of Spatial Inlet Temperature and Pressure Distortion on Turbofan Engine Stability. Technical report, Amerian Institute of Aeronautics and Astronautics - AIAA, 7 1988. 24th Joint Propulsion Conference.

[29] GE Aviation. The GE90 Engine. https://www.geaviation.com/.

[30] MTU Aero Engines. TP400-D6. https://www.mtu.de/.

[31] Airbus. Putting "teeth" in Europe's front-line combat aircraft. https://www.airbus.com/.

[32] Sherri Lynette Smith. One-Dimensional Mean Line Code Technique to Calculate Stage-by-Stage Compressor Characteristics. Master's thesis, The University of Tennessee, 5 1999.

[33] Yogi Sheoran, Milt Davis, and Dave Beale. Integrated test and evaluation techniques as applied to an inlet swirl investigation using the F109 gas turbine engine. *ASME Turbo Expo 2008: Power for Land, Sea and Air*, 6 2018.

[34] R.C.W. de Koning. Development of a Parametric 3D Turbomachinery Blade Modeler. Master's thesis, TU Delft, 8 2015.

[35] Max J. Miller. Estimation of deviation angle for axial-flow compressor blade sections using inviscid-flow solutions. Technical report, National Aeronautics and Space Administration - NASA, Lewis Research Center, 3 1974.